nature structural & molecular biology

Article

https://doi.org/10.1038/s41594-024-01228-3

The open gate of the AMPA receptor forms a Ca^{2+} binding site critical in regulating ion transport

Received: 8 April 2023

Accepted: 18 January 2024

Published online: 26 February 2024

Check for updates

Terunaga Nakagawa [1,2,3] ✉, Xin-tong Wang [4,5], Federico J. Miguez-Cabello[4] & Derek Bowie [4]

Alpha-amino-3-hydroxyl-5-methyl-4-isoxazole-propionic acid receptors (AMPARs) are cation-selective ion channels that mediate most fast excitatory neurotransmission in the brain. Although their gating mechanism has been studied extensively, understanding how cations traverse the pore has remained elusive. Here we investigated putative ion and water densities in the open pore of Ca^{2+}-permeable AMPARs (rat GRIA2*flip*-Q isoform) at 2.3–2.6 Å resolution. We show that the ion permeation pathway attains an extracellular Ca^{2+} binding site (site-G) when the channel gate moves into the open configuration. Site-G is highly selective for Ca^{2+} over Na^{+}, favoring the movement of Ca^{2+} into the selectivity filter of the pore. Seizure-related N619K mutation, adjacent to site-G, promotes channel opening but attenuates Ca^{2+} binding and thus diminishes Ca^{2+} permeability. Our work identifies the importance of site-G, which coordinates with the Q/R site of the selectivity filter to ensure the preferential transport of Ca^{2+} through the channel pore.

AMPARs mediate most of the fast excitatory synaptic transmission in the central nervous system[1]. The neurotransmitter L-glutamate activates postsynaptic AMPARs, which triggers channel gating and ion permeation, causing dendritic membrane depolarization. AMPARs are non-selective cation channels that are able to permeate various cations; however, Na^{+} and Ca^{2+} are the main permeating ions in the context of synaptic transmission. Ca^{2+}-permeable and Ca^{2+}-impermeable AMPARs (CP- and CI-AMPARs) are present in the brain, typically associated with auxiliary subunits that modulate their function[2]. CP-AMPARs regulate neuronal excitability but also transport the second messenger Ca^{2+} to augment signal transduction[3]. Although they are less abundant than CI-AMPARs, CP-AMPARs are critical for synaptic plasticity underlying learning and addiction, excitatory synaptic transmission at the afferent synapses of inhibitory neurons and synaptic maintenance mediated by glial cells, while their dysfunctions are related to developmental epilepsy, glioma, amyotrophic lateral sclerosis and excitotoxicity[3]. Despite the importance of elucidating brain physiology and designing therapeutics that could control synaptic activity, the structural basis for ion permeation in AMPARs remains elusive.

The AMPAR ion channel assembles as homo-tetramers or hetero-tetramers of homologous subunits GluA1–GluA4 (ref. 2); each subunit consists of an amino-terminal domain (NTD), a ligand-binding domain (LBD), a transmembrane domain (TMD) and a cytoplasmic domain (Fig. 1a). The NTD and LBD build the pseudo-twofold symmetric extracellular architecture, while the TMDs form a pseudo-fourfold symmetric ion channel[4–6]. The TMD contains three membrane-spanning helices (M1, M3 and M4), a re-entrant helix (M2) and a selectivity filter (SF). The pore is made exclusively by the M2, M3 and SF (Fig. 1b–d). At the extracellular entrance of the pore, the M3 helices converge and form the channel gate. Binding of L-glutamate to the LBD induces a

[1]Department of Molecular Physiology and Biophysics, Vanderbilt University, School of Medicine, Nashville, TN, USA. [2]Center for Structural Biology, Vanderbilt University, School of Medicine, Nashville, TN, USA. [3]Vanderbilt Brain Institute, Vanderbilt University, School of Medicine, Nashville, TN, USA. [4]Department of Pharmacology and Therapeutics, McGill University, Montreal, Quebec, Canada. [5]Integrated Program in Neuroscience, McGill University, Montreal, Quebec, Canada. ✉e-mail: terunaga.nakagawa@vanderbilt.edu

https://doi.org/10.1038/s41594-024-01228-3

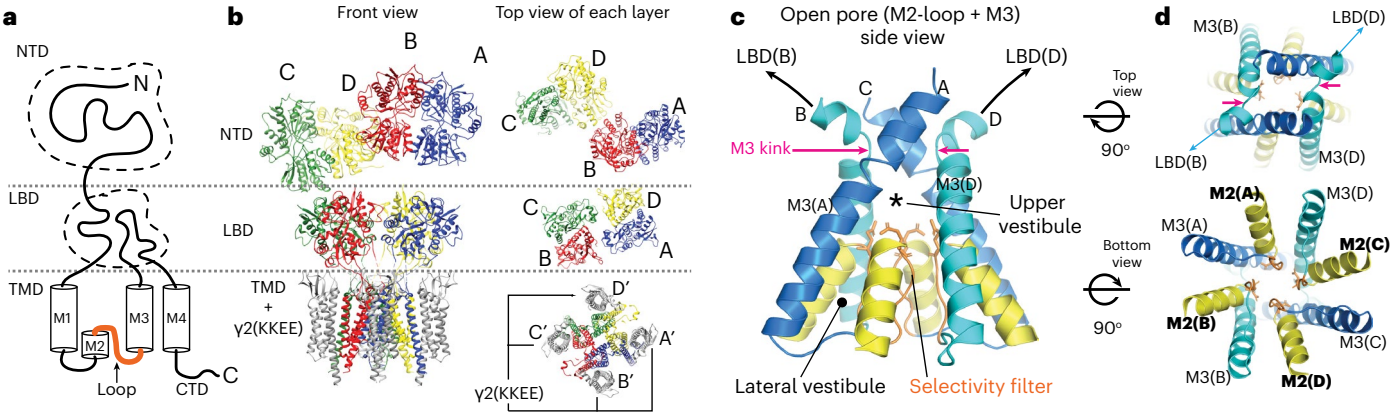

e

Cryo-EM structures	Na^+ (mM)	Ca^{2+} (mM)	Mg^{2+} (mM)	$NMDG^+$ (mM)	Resolution[a] (Å)	PDB, EMDB[b]
Open-Na110	110	–	–	140	2.34	8FQ5, 29378
Open-Na260	260	–	–	–	2.29	8FQF, 29386
Open-Na610	610	–	–	–	2.40	8FP4, 29359
Open-Ca10	110	10	–	140	2.36	8FQB, 29382
Open-CaNaMg	260	10	1	–	2.44	8FP9, 29360
Open-CaNaMg/N619K	260	10	1	–	2.38	8FPS, 29369
Open-Ca150	110	150	–	–	2.59	8FQ1, 29737
Closed-CaNaMg	150	10	1	–	2.32	8FPG, 29363

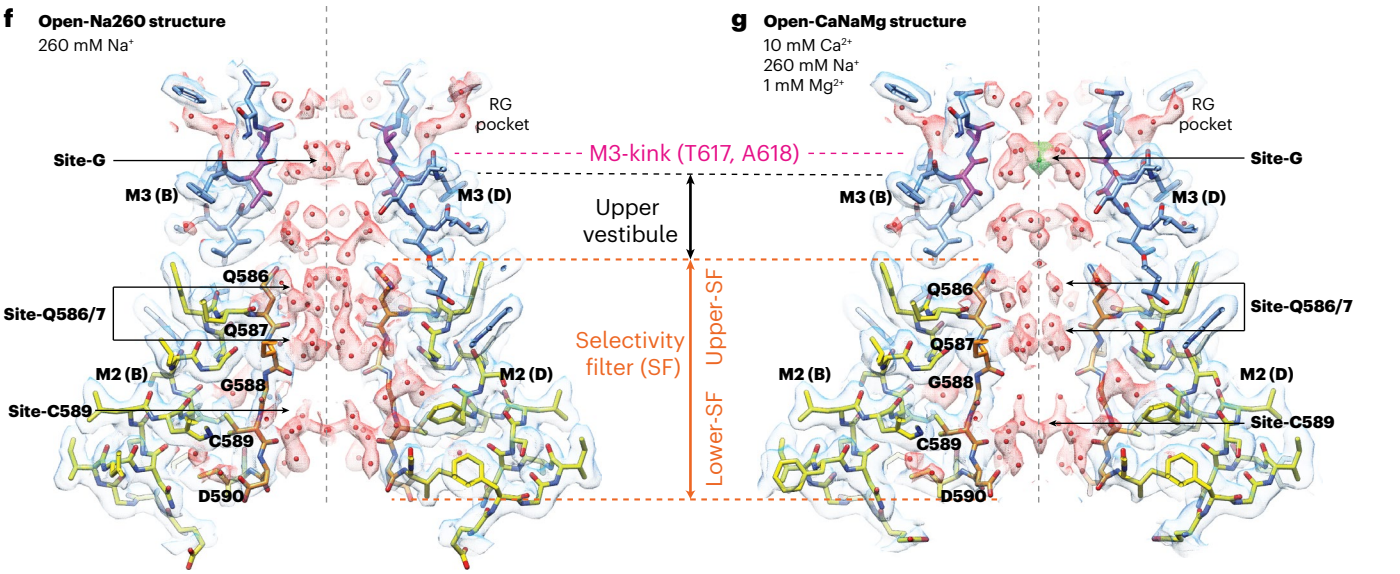

Fig. 1 | The ion permeation path of A2iQ/γ2(KKEE). a, Domain organization of an AMPAR subunit. The orange loop contains the SF. CTD, cytoplasmic domain. **b**, Tetrameric assembly of A2iQ/γ2(KKEE), whose global structure is indistinguishable from the WT complex. GluA2 subunits; A, blue; B, red; C, green; D, yellow. Four γ2(KKEE)s are in gray and their positions are labeled A′, B′, C′ and D′. **c**, Architecture of the open pore. M3 of A/C subunits is in blue; M3 of B/D subunits is in cyan; M2 is yellow; SF is orange. **d**, Top: the open pore viewed from the extracellular space. Bottom: the SF viewed from the cytoplasmic side. **e**, Summary of ion conditions used in each cryo-EM structure. [a]C2 map resolutions of the transmembrane region are listed. See Table 1 and Supplementary Table 1 for details of refinement statistics. [b]PDB and EMDB codes are for the transmembrane region. **f**,**g**, The central slices of the pore of Open-Na260 (**f**, map threshold, 6.0σ) and Open-CaNaMg (**g**, map threshold, 3.3σ). The cryo-EM density map (mesh) and the atomic model are superimposed. Putative water molecules and Ca^{2+} are in red and green spheres, respectively. Regions of intense density accumulation are indicated as site-G, site-Q586/7 and site-C589. Dashed gray lines are pore symmetry axes. The RG pocket indicates a cavity filled with water that is on the rear side of site-G and commonly found in the open structures.

domain closure that transduces to the TMD[7–11], which dilates the gate into a twofold symmetric architecture[9–11] (Fig. 1c,d). According to the symmetry, the B/D (or A/C) subunits are geometrically equivalent[4] (Fig. 1b). The LBDs in the B/D subunits are pivotal for dilation, as they pull and kink the M3, whereas the M3 remains straight in the A/C subunits (Fig. 1c,d)[9–11]. The ion permeation path below the gate is subdivided into the upper vestibule and the SF (Fig. 1c), and the SF is surrounded by the lateral vestibule (Fig. 1c).

CI-AMPARs arise from RNA editing that converts the encoding of amino acid at the Q/R site in the SF of GluA2 (residue 586 in rat) from neutral glutamine (Q) to a positively charged arginine (R)[3,12]. The unedited homotetrameric GluA2*flip*(Q) isoform (A2iQ), a frequently used model for the CP-AMPAR, has a linear current–voltage relationship in the absence of polyamines[13]. When the permeating cations on both sides of the membrane are the same, the AMPAR conductance is near identical at a wide range of voltages with a reversal

https://doi.org/10.1038/s41594-024-01228-3

Table 1 | Cryo-EM data collection, refinement, and validation statistics

	Open-Na260,TMD-STG (EMDB-29386)(PDB 8FQF)		Open-CaNaMg,TMD-STG (EMDB-29360)(PDB 8FP9)		Open-Ca150,TMD-STG (EMBD-29737)(PDB 8FQ1)		Open-Na610,TMD-STG (EMDB-29359)(PDB 8FP4)	
Data collection and processing								
Magnification	105,000x		130,000x		130,000x		105,000x	
Voltage (kV)	300		300		300		300	
Electron exposure (e–/Å^2)	51		50		50		50	
Defocus range (μm)	−0.7 to -2.1		−0.5 to −1.5		−0.8 to −2.0		−0.8 to −2.0	
Pixel size (Å)	0.820		0.8195[#]		0.8195[#]		0.820	
Energy filter band width (eV)	20		15		20		20	
Number of micrographs	16,096		32,662		28,472		23,493	
Initial particle images (no.)	5,409,247		5,075,710		5,573,868		5,140,390	
Final particle images (no.)	1,093,405		822,038		540,796		901,154	
Symmetry imposed	C1	C2	C1	C1	C2	C2	C1	C2
Map resolution (Å)	2.38	2.29	2.59	2.50	2.40	2.44	2.78	2.59
Map resolution with LBD* (Å)	2.50	ND	2.63	2.57	2.46	2.57	2.84	2.73
FSC threshold	0.143	0.143	0.143	0.143	0.143	0.143	0.143	0.143
Map resolution range (Å)	2.3-3.7	2.2-3.5	2.5-4.1	2.4-3.9	2.3-3.9	2.4-3.8	2.6-4.3	2.5-4.1
Refinement (C2) ^								
Initial model used (PDB code)	5WEO		5WEO		5WEO		5WEO	
Model resolution (Å)	2.0/2.3 (masked)		2.2/2.5 (masked)		2.2/2.7 (masked)		2.2/2.4 (masked)	
FSC threshold	0.143/0.5		0.143/0.5		0.143/0.5		0.143/0.5	
Map sharpening *B* factor (Å^2)	−56.0		−69.5		−72.1		−70.8	
Model composition								
Non-hydrogen atoms	10,895		10,851		10,876		10,876	
Protein residues	1,366		1,366		1,366		1,366	
Ligands	CL:2		CA:1, CL:4		CA:2		CL:2	
Water	231		190		170		218	
B factors (Å^2)								
Protein	38.03		57.87		55.01		40.64	
Ligand	59.77		76.98		87.40		73.02	
Water	25.84		44.19		45.02		36.14	
R.m.s. deviations								
Bond lengths (Å)	0.002		0.002		0.002		0.002	
Bond angles (°)	0.428		0.478		0.403		0.421	
Validation								
MolProbity score	1.30		1.13		1.21		1.36	
Clashscore	4.62		3.35		3.70		4.15	
Poor rotamers (%)	0.54		0.98		1.17		1.25	
Ramachandran plot								
Favored (%)	97.72		98.03		98.01		97.57	
Allowed (%)	2.28		1.97		1.99		2.43	
Disallowed (%)	0.00		0.00		0.00		0.00	

	Open-Ca10,TMD-STG (EMDB-29382)(PDB 8FQB)	Open-Na110,TMD-STG (EMBD-29378)(PDB 8FQ5)	Open-CaNaMg/N619K, TMD-STG (EMDB-29369)(PDB 8FPS)	Closed-CaNaMg,TMD-STG (EMDB-29363)(PDB 8FPG)
Data collection and processing				
Magnification	130,000x	130,000x	130,000x	130,000x
Voltage (kV)	300	300	300	300
Electron exposure (e–/Å^2)	53	52	54.6	56
Defocus range (μm)	−0.8 to −2.0	−0.6 to -2.0	−0.8 to -2.0	−0.8 to −1.8

https://doi.org/10.1038/s41594-024-01228-3

Table 1 (continued) | Cryo-EM data collection, refinement, and validation statistics

	Open-Ca10,TMD-STG (EMDB-29382)(PDB 8FQB)		Open-Na110,TMD-STG (EMBD-29378)(PDB 8FQ5)		Open-CaNaMg/N619K, TMD-STG (EMDB-29369)(PDB 8FPS)		Closed-CaNaMg,TMD-STG (EMDB-29363)(PDB 8FPG)	
Pixel size (Å)	0.8195#		0.8195#		0.8195#		0.8195#	
Energy filter band width (eV)	20		20		20		15	
Number of micrographs	28,505		30,384		34,729		34,553	
Initial particle images (no.)	7,059,177		4,655,266		6,655,184		3,905,978	
Final particle images (no.)	986,075		692,680		693,935		847,436	
Symmetry imposed	C1	C2	C1	C2	C1	C2	C1	C2
Map resolution (Å)	2.48	2.36	2.42	2.34	2.48	2.36	2.42	2.34
Map resolution with LBD* (Å)	2.52	2.44	2.46	2.38	2.52	2.44	2.46	2.38
FSC threshold	0.143	0.143	0.143	0.143	0.143	0.143	0.143	0.143
Map resolution range (Å)	2.4-4.1	2.3-3.9	2.3-4.0	2.2-3.7	2.4-4.1	2.3-3.9	2.3-4.0	2.2-3.7
Refinement (C2) ^								
Initial model used (PDB code)	5WEO		5WEO		5WEO		5WEO	
Model resolution (Å)	2.1/2.5 (masked)		2.1/2.4 (masked)		1.9/2.6 (masked)		2.0/2.4 (masked)	
FSC threshold	0.143/0.5		0.143/0.5		0.143/0.5		0.143/0.5	
Map sharpening *B* factor (Å^2)	−64.9		-58.3		−62.8		−62.0	
Model composition								
Non-hydrogen atoms	10,823		10,876		10,602		10,674	
Protein residues	1,366		1,366		1,338		1,348	
Ligands	CA:1, CL:2		CL:4		CL:4		CL:4	
Water	176		220		152		187	
B factors (Å^2)								
Protein	41.01		39.99		35.33		42.86	
Ligand	75.39		63.98		66.30		71.43	
Water	33.39		37.15		27.41		38.77	
R.m.s. deviations								
Bond lengths (Å)	0.002		0.002		0.002		0.003	
Bond angles (°)	0.451		0.441		0.370		0.489	
Validation								
MolProbity score	1.45		1.23		1.12		1.73	
Clashscore	4.96		3.44		3.32		4.90	
Poor rotamers (%)	1.79		1.16		1.01		1.84	
Ramachandran plot								
Favored (%)	98.10		97.80		98.76		96.00	
Allowed (%)	1.90		2.20		1.24		4.00	
Disallowed (%)	0.00		0.00		0.00		0.00	

The pixel size (Å) was 0.647 at the detector level prior to binning. * Resolution of the map generated by focused refinement of the LBD-TMD-STG. ^ Model refinement was conducted against the C2 map of TMD-STG. ND, not determined

potential of 0 mV. Therefore, in the absence of voltage, the distribution of permeating cations and water in the open pore is predicted to provide critical insights into the mechanism of conductance and ion permeation[14,15].

Cryogenic-electron microscopy structures of the open pore

To facilitate, and potentially stabilize, the energetically unstable open state, the wild type (WT) A2iQ was co-expressed with the K52E/K53E (KKEE) mutant of auxiliary subunit TARPγ2 (γ2), which substantially slows the rate of AMPAR desensitization[16]. The KKEE mutations are in the flexible extracellular β1–β2 loop, unresolved in all TARP structures but predicted to make transient contacts with the LBD[9,11,17,18]. To capture the open pore conformation, the agonist (100 mM L-glutamate) and an inhibitor of desensitization (330 μM cyclothiazide (CTZ)) were co-applied to the purified receptor before vitrification. The cryogenic-electron microscopy (cryo-EM) structures, at an overall resolution in the range of 2.28–2.59 Å, were obtained in various concentrations of Na^+ and Ca^{2+} to identify ion-specific features (Table 1, Extended Data Figs. 1–4 and Supplementary Table 1). It was critical to use a large number of particles, approximately 600,000–1,000,000 particles, in the final refined map to reveal the signals of non-protein features in the open pore. When necessary, NMDG was supplemented to maintain ionic strength (Fig. 1e). The large $NMDG^+$ cation permeates AMPAR substantially less (~2%) than small cations[19], and thus the probability of finding $NMDG^+$ in the pore is expected to drop accordingly and be negligible.

The specific cation conditions examined (followed by the name of the obtained structure) are as follows: 110 mM Na^+/140 mM $NMDG^+$ (Open-Na110); 260 mM Na^+ (Open-Na260); 610 mM Na^+ (Open-Na610); 10 mM Ca^{2+}/110 mM Na^+/140 mM $NMDG^+$ (Open-Ca10); 10 mM Ca^{2+}/260 mM Na^+/1 mM Mg^{2+} (Open-CaNaMg); and 150 mM Ca^{2+}/110 mM Na^+ (Open-Ca150) (Fig. 1e). The concentrations listed above include the extra 110 mM Na^+ from the agonist solution because the L-glutamate stock solution is titrated at pH 7.4 using NaOH (Methods). For example, the particles in Open-Na110 were purified in 140 mM $NMDG^+$, and adding the L-glutamate stock solution that contains Na^+ made the final ionic condition of 110 mM Na^+/140 mM $NMDG^+$ (see Methods for other conditions). Some conditions contained 1 mM Mg^{2+} but its effect was not systematically explored. Additionally, a reference structure of the closed state (Closed-CaNaMg) was obtained in the presence of antagonist (100 μM CNQX) and 330 μM CTZ in 10 mM Ca^{2+}/150 mM Na^+/1 mM Mg^{2+}.

The architectures of the complexes in both the open and closed states were at the stoichiometry of A2iQ:γ2(KKEE) = 4:4 and agree with the WT complex[10] (Fig. 1b and Extended Data Fig. 5f–h). The extracellular region spanning the KKEE mutations is flexible and unresolved like the WT (Extended Data Fig. 1g,h). Gating is accompanied by global motions of the γ2(KKEE) equivalent to those observed in TARPγ8 (ref. 11) (Extended Data Fig. 5i–n). The core gating machinery of the A2iQ/γ2(KKEE) complex is virtually identical to the WT complexes[9,10]. In all open structures, the LBDs were closed and fully occupied with CTZ and L-glutamate. The dimer-of-dimers organization of the tetrameric LBD (LBD gating ring) adopts alternative architectures characterized by small displacements between the two LBD dimers (Extended Data Fig. 5a–e and Supplementary Table 1), consistent with the mobile nature of the LBDs. The cytoplasmic half of the SF, at residues G588 and C589, was more flexible than the surroundings based on the lower local resolution (Extended Data Fig. 3i–l). Consistently, alternative side chain orientation was observed at C589 under a subset of ion conditions.

Identification of a new Ca^{2+} binding site

Numerous non-protein densities occupy the gate, vestibules and SF (Fig. 1f–g and Extended Data Figs. 6 and 7), with the majority being interpreted as putative water molecules, although we cannot fully exclude the possibility that some are ions or even noise. The large densities at site-G (that is, at the gate residues T617/A618) as well as at site-Q586/7 and site-C590 within the SF (Fig. 1f,g), if present, were consistent in the half-maps and regardless of applying C2 symmetry (Extended Data Figs. 3 and 4). In fact, the density accumulation at the upper SF, around site-Q586/7, has been observed in previously reported open structures that were resolved at around 3–3.5 Å resolution[10,20]. With improved resolution, we extend the previous observations and find that the pore-occupying densities in the upper SF often form parallel vertical columns (Fig. 1f and Extended Data Figs. 6 and 7), indicative of energetically equivalent ion conduction pathways, contrasting with the single-file configuration observed in potassium channels[14]. The distribution of putative ion and water density within the SF was variable, between ion condition and morphologically complex (Fig. 1f,g and Extended Data Figs. 6 and 7), making it difficult to identify features that are specific to any cations. By contrast, the positions of many putative water molecules in the lateral vestibule match between structures, highlighting their common accumulation points (Extended Data Fig. 8). The distribution of the putative water molecules in the lateral vestibule may suggest their role in providing structural flexibility to the SF.

Although it was challenging to interpret the non-protein densities in the lower ion permeation path, robust cation-specific features were identifiable at the upper element of the pore. The central pore axis density at site-G was present only in ionic conditions that included Ca^{2+} (that is, Open-Ca10, Open-CaNaMg and Open-Ca150), regardless of imposing symmetry, while the surrounding polypeptides adopt virtually identical conformations in all cases (Fig. 2a–f,h and Extended Data Fig. 4c–e). Therefore, the correlation between the density and ion composition suggests that the central density contains Ca^{2+}. The higher local resolution of the density in 150 mM Ca^{2+} (Open-Ca150) compared with 10 mM Ca^{2+} (Open-Ca10 and Open-CaNaMg) is consistent with more stable Ca^{2+} binding at site-G at higher Ca^{2+} concentrations (Extended Data Fig. 3i–k). Although the central density should be regarded as an ensemble of Ca^{2+} and water because of their dynamic nature and the limited resolution, it is possible to place a Ca^{2+} surrounded by four waters at 2.4 Å spacing, partially fulfilling the requirements for the hydration shell[21] (Fig. 2h,i). Importantly, the central pore-occupying density at site-G did not emerge even when the Na^+ concentration was raised from 110 mM (in Open-Na110) to 610 mM (in Open-Na610) (compare Fig. 2c and 2e), indicative of high selectivity of site-G for Ca^{2+} over Na^+. In the open-gate conformation, site-G is located immediately outside of the membrane, thus it may be viewed as an extracellular vestibule immediately outside of the membrane electric field. The vestibule is formed only in the open state, and thus site-G is a transient state-dependent Ca^{2+} binding site (Extended Data Fig. 6a–c,h). Furthermore, site-G is in the carboxy-terminal portion of the M3 helix encoded by the evolutionarily conserved amino acid sequence SYTANLAAF, making it likely to be a common structural element in almost all ionotropic glutamate receptors (iGluRs) (Fig. 2g).

External Ca^{2+} block predicted from the open structures

Given that 10 mM Ca^{2+} can dominate the occupancy of site-G even in the presence of excess Na^+ (Fig. 2a,b), we postulated that Ca^{2+} binding to site-G would cause a block by excluding Na^+ from entering the pore. Given that site-G lies outside the membrane electric field, the mechanism of the block would be expected to be voltage-independent. To test this supposition, we recorded steady-state membrane currents evoked by 10 mM L-glutamate with 100 μM CTZ on outside-out patches expressing A2iQ/γ2 receptors using an external solution of 150 mM NaCl with varying concentrations of added Ca^{2+} (0.1–108 mM). L-glutamate was applied in the presence of cyclothiazide (100 μM) to attenuate AMPAR desensitization, and the steady-state response observed at each concentration of external Ca^{2+} was ramped from −100 mV to +100 mV. As anticipated, we observed a block of AMPAR-mediated membrane currents by external Ca^{2+} in a dose-dependent manner over a wide range of membrane potentials (Fig. 3a). At −100 mV, the apparent affinity for inhibition (half-maximum inhibitory concentration, IC_{50}) and steady-state response (G_{min}) was estimated to be 5.21 ± 0.64 mM and 19.67% (n = 8), respectively (Fig. 3b and Supplementary Table 2). Interestingly, although site-G is in an extracellular location, the external Ca^{2+}-block was voltage-dependent and the data points were well fit by a single permeant ion blocker model[22] with an estimated dissociation constant ($K_{d(0mV)}$) of 3.2 mM at physiological Ca^{2+} levels (Fig. 3c and Supplementary Table 3). This latter point suggests that external Ca^{2+} not only impedes the flow of Na^+ at site-G but also hinders Na^+ permeation at another location within the membrane that is sensitive to voltage. In keeping with this idea, there is a large density accumulation in the SF of Open-Ca150 (Extended Data Figs. 6c and 7c), implying that the SF also traps Ca^{2+} that interferes with the passage of Na^+, accounting for the voltage-dependent component of the Ca^{2+} block.

To explore this point further, we repeated experiments with Ca^{2+}-impermeable GluA2*flip*(R)/TARPγ2 (A2iR/γ2) receptors, which do not permeate Ca^{2+} beyond the SF but may allow Ca^{2+} to access and bind to site-G. Here, we observed that external Ca^{2+} was still effective in blocking A2iR-mediated Na^+ currents (Fig. 3e), though the mechanism was now voltage-independent (Fig. 3f). The apparent affinity for inhibition (IC_{50}, 11.27 ± 0.93 mM, n = 6) was lower, suggesting that there may be coupling between site-G and the SF in A2iQ/γ2 receptors, or alternatively, that the R586 residue may weaken the Ca^{2+} affinity at site-G in A2iR/γ2 receptors. Conductance was negligible at the highest Ca^{2+} concentration (108 mM), which would be expected given that A2iR receptors poorly conduct Ca^{2+} (Fig. 3e and Supplementary Table 2).

https://doi.org/10.1038/s41594-024-01228-3

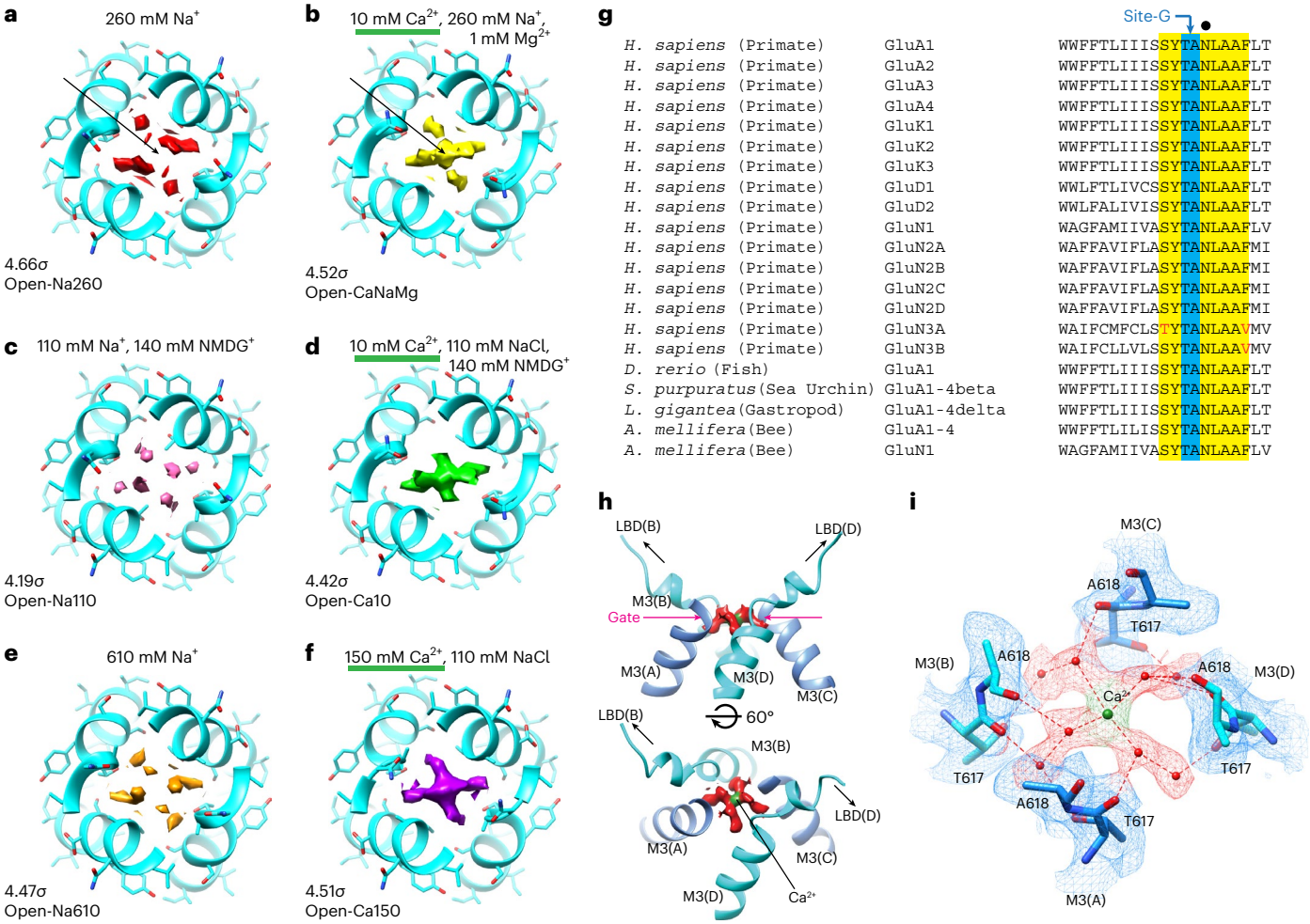

Fig. 2 | Site-G as a Ca^{2+} binding site at the gate. a–f, Top views of site-G in the open gates under different ionic conditions. The M3 helices are in cyan. Pore-occupying densities are in red (Open-Na260) (**a**), yellow (Open-CaNaMg) (**b**), pink (Open-Na110) (**c**), green (Open-Ca10) (**d**), orange (Open-Na610) (**e**) and purple (Open-Ca150) (**f**). The sigma values indicate display thresholds. Overall density occupying site-G is stronger when Ca^{2+} is present. For example, compare the arrows in **a** and **b**. See Extended Data Figs. 6 and 7 for side view. **g**, Alignment spanning the SYTANLAAF motif. Atypical residue in red. The non-vertebrate subunit nomenclature follows a previous publication[49]. **h**, Side (top) and diagonal (bottom) view of site-G in Open-CaNaMg. The M3 helices in cyan and blue. The EM density map of putative water and putative Ca^{2+} are in red and green, respectively. **i**, T617 and A618 form site-G. The atomic model and density map are superimposed. The dashed red lines are the putative hydrogen bonds and ion–water interactions.

Collectively, both voltage-dependent and voltage-independent mechanisms contribute to the external Ca^{2+} block of A2iQ receptors, consistent with the involvement of an upper vestibular structure, site-G, that lies outside the electrostatic field generated by the membrane potential.

The N619K mutation reveals site-G function

To further test whether the Ca^{2+} block is mediated by site-G, the N619 residue (Fig. 2g, black dot) adjacent to site-G was interrogated. The N619K mutation in GluA2 corresponds to a seizure-related N650K mutation in the GluN1 subunit of the NMDA receptor (NMDAR)[23]. The cryo-EM structure of N619K mutation of A2iQ in complex with γ2(KKEE) (Open-CaNaMg/N619K), in the same ionic condition as the WT (Open-CaNaMg) (Figs. 1e and 4a), revealed that its open conformation lacks the M3 kink present in the WT receptor (Fig. 4b, black arrowhead, Extended Data Figs. 2m,n, 6g, and 7g, Table 1 and Supplementary Table 1), while the predicted pore radius along the permeation path was similar (Extended Data Fig. 9). In the B/D subunits of WT, a cavity with a density that can accommodate three water molecules is found at the rear side of site-G next to N619 (RG pocket), contributing to the M3 kink by disrupting the α-helix fold (Fig. 4b and Extended Data Fig. 7a–f). The mutated residue, K619, is space-occupying and prevents the RG pocket from forming, which may keep the M3 intact (Fig. 4a and Extended Data Fig. 7g).

Focused classification and refinement of the LBD gating ring (Fig. 4d) revealed that the LBDs are fully liganded like the WT, but the mutant gate adopts an alternative open conformation (Fig. 4a). Substituting the intrinsically dynamic water in the RG pocket with the well-structured side chain of K619, which is greater in size than the N619 in WT (Fig. 4a,b), may contribute to stabilizing the alternative open conformation in the N619K mutant complex. In fact, the N619K mutant A2iQ bound to γ2 (N619K/γ2) spontaneously opens to about 30% of the peak agonist response (Fig. 5a,d, Extended Data Fig. 10a–f and Supplementary Tables 4–6). Interestingly, the leak current was weakly sensitive to AMPAR antagonists, GYKI-52466 and NBQX (Extended Data Fig. 10g–l and Supplementary Tables 4–6), as well as being sensitive to block by cytoplasmic spermine, which is a hallmark of the open pore of the AMPAR (Extended Data Fig. 10a–f). Unlike γ2-bound WT A2iQ (WT/γ2), the N619K/γ2 receptors fail to desensitize in the continued presence of the agonist and exhibit slow agonist off-kinetics, suggesting that they have a much higher affinity for L-glutamate (Fig. 5a–f). Interestingly, the leak and agonist-evoked responses of the N619K/γ2 receptor have differing affinities and voltage-sensitivity to cytoplasmic polyamine block, suggesting that the N619K mutation profoundly

https://doi.org/10.1038/s41594-024-01228-3

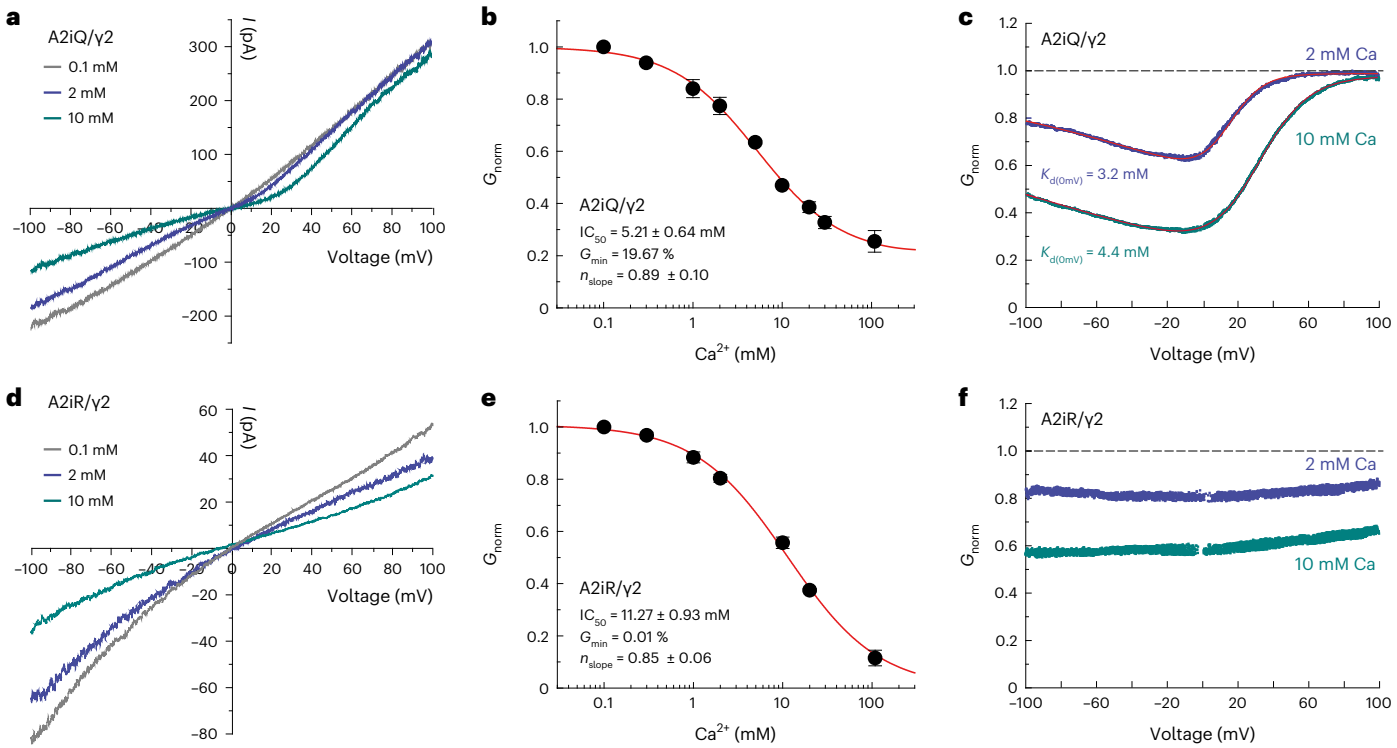

Fig. 3 | External Ca^{2+} block of GluA2/γ2 and its voltage dependence. **a**,**d**, Current records observed in the presence of 10 mM glutamate and 100 µM CTZ at a voltage range of −100 mV to +100 mV in the presence of 0.1 mM (gray), 2 mM (light blue) and 10 mM (dark blue) Ca^{2+} for A2iQ/γ2 (patch no. 220914p7) (**a**) and A2iR/γ2 (patch no. 221025p2) (**d**) receptors. **b**,**e**, Inhibition plots of block by external Ca^{2+} of A2iQ/γ2 ($n = 8$) (**b**) and A2iR/γ2 ($n = 6$) (**e**) receptors at −100 mV. Data are presented as mean values ± s.e.m. **c**,**f**, Conductance–voltage plots of a block by 2 mM or 10 mM external Ca^{2+} of A2iQ/γ2 (**c**) and A2iR/γ2 (**f**) receptors. The voltage dependence of the block of A2iQ/γ2 receptors was well fit by a single permeant ion blocker model (red line), whereas the block of A2iR/γ2 receptors was voltage insensitive.

affects ion transport through the pore (Extended Data Fig. 10b,c,e,f and Supplementary Table 7).

A closer examination of site-G in the N619K mutant reveals that it is narrower in the B/D subunit axis (distances of T617 Cα of B/D: 12.38 Å in N619K vs 13.57 Å in WT) and wider in the A/C axis (distances of T617 Cα of A/C: 11.84 Å in N619K vs 11.56 Å in WT) compared with the WT (Fig. 4c). These structural changes were correlated with the absence of a central Ca^{2+} density, with the mutant lacking the structural signature for Ca^{2+} binding to site-G (Fig. 4a,b). In keeping with this, external Ca^{2+} exhibited a substantially reduced ability to block both the leak and agonist-evoked responses of N619K/γ2 receptors, with G_{min} values of 52.18% (leak) and 66.07% (agonist) ($n = 6$), respectively (Fig. 5g–j and Supplementary Table 2). The residual external Ca^{2+} block in N619K/γ2 may be caused by the interaction between the Ca^{2+} and elements in the ion permeation pathway other than site-G. Considering that the external Ca^{2+} block is only weakly voltage-dependent in the N619K/γ2 (Fig. 5j) and that the polyamine sensitivity is substantially altered in N619K/γ2 compared with WT/γ2 (Extended Data Fig. 10), as described above, there may be a weak voltage-dependent interaction between Ca^{2+} and the SF of N619K/γ2 that is contributing to the residual external Ca^{2+} block. Long-range allosteric coupling between the architectures surrounding the gate and the M2 (ref. 11,20), which is adjacent to the SF, could potentially explain the mechanism by which the cytoplasmic polyamine block affinity is affected in the N619K mutant.

Importantly, the mutant N619K/γ2 receptors exhibited markedly reduced Ca^{2+} permeability compared with WT/γ2 receptors (Fig. 6 and Supplementary Table 8), with an estimated P_{Ca2+}/P_{Na+} ratio of 0.32 ± 0.04 ($n = 10$) for N619K/γ2 receptors compared with 5.28 ± 0.21 ($n = 8$) for WT/γ2 receptors (unpaired t-test, $P < 0.001$; Fig. 6d and Supplementary Table 8), which is consistent with the observation in GluA2 receptors expressed in the absence of auxiliary subunits[24]. The K619 side chains point away from the pore, their negatively charged ε-amino group (pKa = 9.5) is engaged by the carbonyl oxygens in the S785 residue within a distance of 3 Å and therefore is unlikely to produce strong charge repulsion to the permeating cations (Fig. 4a). Positive charge at position 619 is unlikely to be the determinant because mutating N619 to a neutral cysteine also attenuates Ca^{2+} permeability[24]. Collectively, we suggest that site-G is a Ca^{2+} binding site that is a key determinant of Ca^{2+} permeability in AMPARs.

Discussion

State-dependent Ca^{2+} binding site critical for ion transport

In this work, we present high-resolution cryo-EM structures of the open pore of the AMPAR in complex with the gain-of-function mutant of TARPγ2(KKEE). The difference observed in pore-occupying densities with and without Ca^{2+} revealed a new Ca^{2+} binding site (that is, site-G) at the open gate that lies outside the membrane electric field (Fig. 7). Importantly, site-G is formed only when the channel enters the open state, making it a transient, state-dependent Ca^{2+} binding site. Occupancy of Ca^{2+} at site-G offers a mechanism whereby Ca^{2+} preferentially accumulates at the open gate to ensure Ca^{2+} entry to the pore and SF, even though the physiological extracellular concentration and diffusion coefficient of Ca^{2+} are 70-fold and 2-fold lower than those of Na^{+}, respectively (Fig. 7). Increase in external Ca^{2+} concentration promotes Ca^{2+} occupancy at site-G that, in turn, blocks the passage of Na^{+} (Fig. 7). Furthermore, the function of site-G was disrupted by introducing the N619K mutation immediately next to site-G (Fig. 7). Collectively, site-G offers a structural explanation for the facilitation of Ca^{2+} permeation in CP-AMPAR and the dose-dependent external Ca^{2+} block of AMPARs, which is a new pharmacological observation.

https://doi.org/10.1038/s41594-024-01228-3

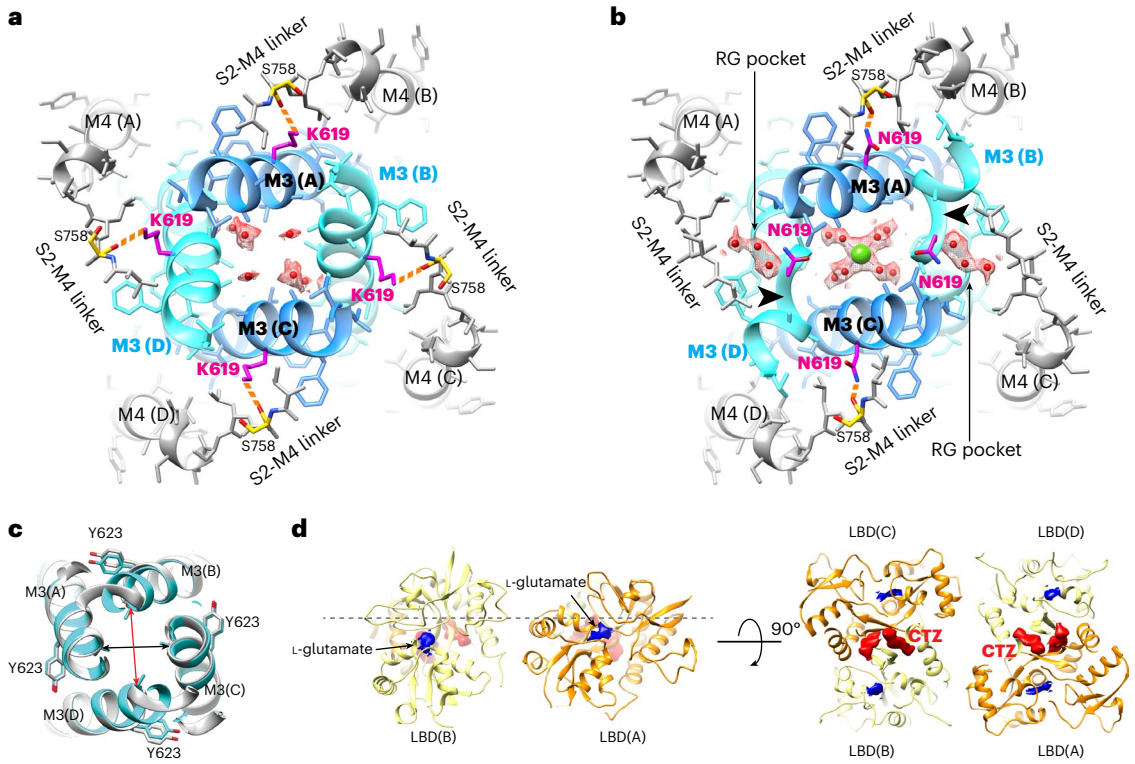

Fig. 4 | N619K mutation reduces Ca^{2+} binding at site-G, external Ca^{2+} block and Ca^{2+} permeability. a,**b**, The site-G of the mutant A2iQ(N619K)/γ2(KKEE) (**a**) and WT A2iQ/γ2(KKEE) (**b**) viewed from the extracellular side. The M3 kink (arrowhead in **b**) is only present in WT. The central pore density is absent in the mutant, and the Ca^{2+} (green sphere) is found in the WT. Water is shown as a red sphere; density map in mesh. The side chains of mutated K619 and the WT counterpart N619 are in magenta. S758 is yellow. K619 interacts with the carbonyl oxygens of S758 (orange dashed lines). In WT, the RG pocket filled with water occupies the space between N619 and S758 in the B/D subunits. In the A/C subunits, N619 interacts with the carbonyl oxygens of S758 (orange dashed lines). **c**, Overlay of site-G of WT (light gray) and N619K (cyan) receptors, aligned using the M3 segment residues 610–615. The pore is narrower in the B/D subunit axis (red arrow: distances of T617 Cα of B/D; 12.38 Å in N619K vs 13.57 Å in WT) and wider in the A/C axis (black arrow: distances of T617 Cα of A/C; 11.84 in N619K vs 11.56 Å in WT). **d**, The ribbon model of the LBD gating ring of LBD conf1 in the A2iQ(N619K)/γ2(KKEE) complex (Supplementary Table 1) displayed in two orthogonal views. LBD monomers of A/C and B/D subunits in orange and light yellow, respectively. The densities for glutamate and CTZ are in blue and red, respectively. The conf2 is also fully liganded as in conf1 (not shown).

Significance of extracellular vestibules in Ca^{2+} permeation

In AMPARs, gate-opening removes the physical obstruction for ion permeation[9–11,20]. This simple view is revised by our identification of site-G in CP-AMPARs. The gate-opening and ion-binding is in fact coupled because the pore dilation not only creates a sieve for ions and water to pass through but also reveals a surface that preferentially captures Ca^{2+} over Na^+, which facilitates Ca^{2+} permeation. More generally, negatively charged surfaces exist at the extracellular vestibules of Ca^{2+}-selective ion channels to efficiently capture extracellular Ca^{2+}, such as seen in the L5 and L6 loops of the calcium channel $Ca_v1.1$[25], the extracellular vestibule of engineered Ca^{2+}-selective bacterial ion channel Ca_vAb[26] and the divalent cation recruitment site (D517, E518 and D547) in the Ca^{2+}-selective transient receptor potential channel V6 (TRPV6)[27]. We suggest that site-G in the AMPAR/γ2 complex performs an analogous role as the Ca^{2+}-accumulating extracellular vestibules found in other Ca^{2+}-selective channels. Given that the gate is highly conserved among all iGluR families (Fig. 2g), site-G may be critical in providing a sufficient influx of Ca^{2+} through Ca^{2+}-permeable iGluRs, such as CP-AMPARs and NMDA receptors (NMDAR), to trigger intracellular signaling[28]. In the case of NMDARs, dilation of the SF and additional Ca^{2+} binding sites are proposed to account for their greater Ca^{2+} permeability compared with AMPARs[29–31].

Site-G and the Q/R site are key determinants of Ca^{2+} permeation

Previous work in AMPARs emphasized the sole role of the Q/R site that sits at the top of the SF in determining Ca^{2+} permeability[28]. Accordingly, recent structural analysis and molecular dynamic simulations have focused on the role of the Q/R site and SF in their modeling and theoretical frameworks[32–34]. However, site-G was not among the ion binding sites predicted by molecular dynamic simulations in the iGluR pore[32,35], which highlights the importance of taking an experimental approach to identifying pore ion binding sites (note: Ca^{2+} binding site 4 in reference[32] differs from site-G). In fact, previous experimental observations have suggested that factors outside of the Q/R site and SF may be critical for Ca^{2+} permeation. First, N619K and N619C mutations in the extracellular vestibule of GluA2, which is adjacent to site-G, substantially attenuate Ca^{2+} permeability[24], indicative of a structural element outside the Q/R site crucial for Ca^{2+} permeability. Second, a hypothetical Ca^{2+} binding site in the upper pore has been proposed to explain the external Ca^{2+} block in NMDARs[36,37]. The postulate was based on the observation that the block was insensitive to applied voltage and, therefore, the hypothetical Ca^{2+} binding site must be outside the membrane electric field. Subsequently, it was shown that the DRPEER motif, present only in the GluN1 subunit and located in the extracellular vestibule, has a substantial role in facilitating Ca^{2+} permeability and captures putative Ca^{2+} before entering the pore[31,38]. However, disruption of the DRPEER motif could not fully eliminate Ca^{2+} permeation, indicating the involvement of another Ca^{2+} binding site[31]. Our work offers an explanation for these findings by providing the structural basis for a Ca^{2+} binding site (that is, site-G) at the vestibule of the AMPAR pore, which is located in the evolutionarily conserved SYTANLAAF motif and upstream of the well-established pore Q/R site in the SF that determines Ca^{2+} permeability[28] (Fig. 7).

https://doi.org/10.1038/s41594-024-01228-3

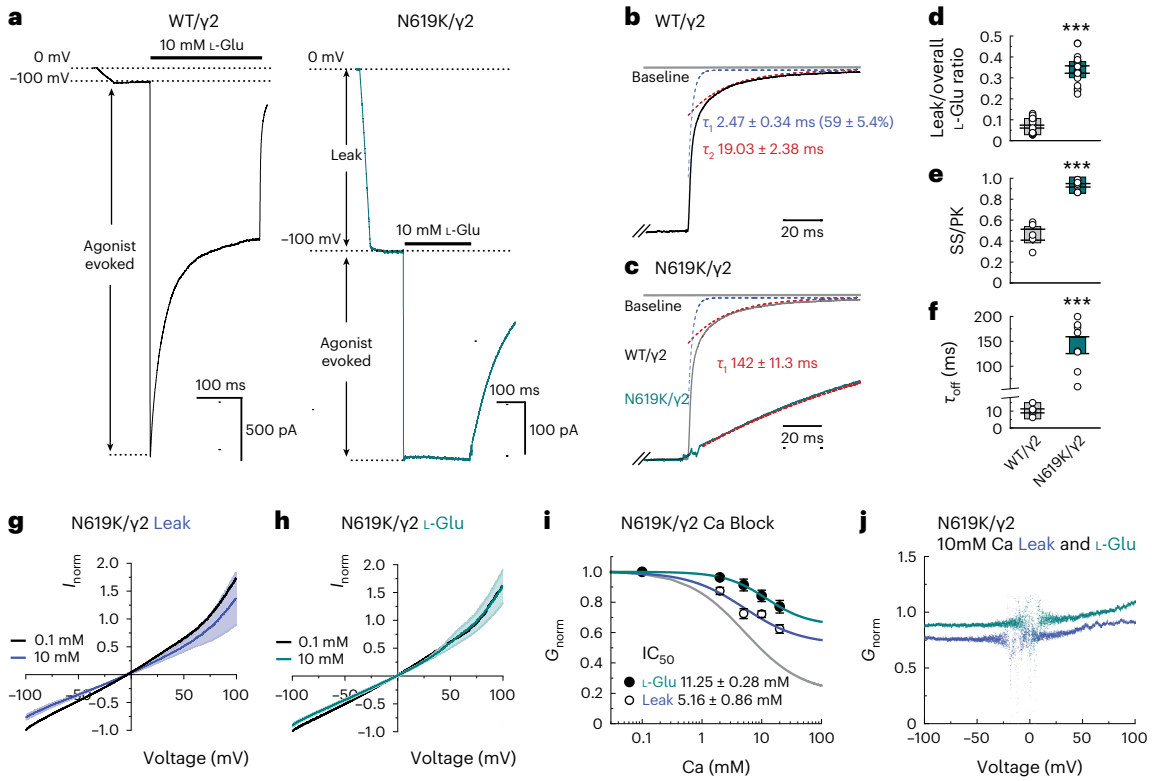

Fig. 5 | N619K mutation promotes opening and alters kinetic properties of the ion channel. a, Example traces of leak and agonist-evoked responses of WT (in black, patch no. 200121p2) and mutant N619K (in cyan, patch no. 221201p5) receptors at −100 mV. Note the substantial leak current in the mutant. **b**, Example of deactivation kinetics of WT (black trace) fit by bi-exponential function (blue and red dashed lines are the τ_1 and τ_2 components, respectively). **c**, Example of deactivation kinetics of N619K superimposed with the WT example from **b**. N619K deactivation kinetics was fit by mono-exponential function. Trace response (cyan) and model fit (red). **d**–**f**, Scatterplots showing all data points from each group. Average represented with gray and cyan squares with s.e.m. **d**, Ratio of leak over overall evoked currents (WT, 0.07 ± 0.01, $n = 6$; N619K, 0.34 ± 0.02, $n = 8$; two-sided Mann–Whitney test, $P < 0.001$). **e**, Steady-state current over peak current ratio (WT, 0.46 ± 0.05, $n = 8$; N619K, 0.93 ± 0.02, $n = 8$; unpaired two-sided t-test with Welch correction, $P < 0.001$). **f**, Deactivation kinetics measured using the offset kinetics. Off kinetics in WT and N619K were fit to bi-exponential (τ_1 and τ_2) and mono-exponential functions, respectively (WT, 10.10 ± 1.18, $n = 6$; N619K, 142.00 ± 11.30, $n = 8$; unpaired two-sided t-test with Welch correction, $P < 0.001$). Also see Supplementary Table 4. **g**,**h**, Normalized I–V currents recorded in N619K/γ2 mutant at holding potential ganging from −100 mV to +100 mV. Black, average response from all recordings in 0.1 mM Ca solution; blue, average responses in 10 mM Ca^{2+} for leak current ($n = 6$); cyan, 10 mM glutamate and 100 µM CTZ evoked responses ($n = 6$); colored shading, s.e.m. **i**, Inhibition plots of external Ca^{2+} block for leak (open circles, $n = 6$) and agonist-evoked (filled circles, $n = 6$) responses in N619K receptors at −100 mV. Data are presented as mean values ± s.e.m. (also see Supplementary Table 3). **j**, Conductance–voltage plots of block by 10 mM external Ca^{2+} for the agonist-evoked curve (cyan) and the leak curve (blue).

Whether the Ca^{2+} block of AMPARs fulfills a physiological role in regulating glutamatergic synapses is not immediately clear. Assuming an extracellular calcium concentration ($[Ca^{2+}]_{ex}$) of 2 mM, which is typical of brain slice experiments, AMPARs would be blocked by about 20%. Measurements have shown that in human brain, the physiological $[Ca^{2+}]_{ex}$ is ~1.2 mM, lower than what is used in slice physiology experiments[39]. The $[Ca^{2+}]_{ex}$ decreases by 0.45 mM in seizures or following high activity[40]. These reported variations in $[Ca^{2+}]_{ex}$ may impact the amplitudes of the AMPAR-mediated response by less than ~10% through the external calcium block reported in this work, which does not offer a sizeable range for regulation. Perhaps a more plausible explanation is that the modest block exerted by physiological levels of Ca^{2+} is a necessary tradeoff to allow the selective transport of Ca^{2+} through the open pore of unedited AMPARs over the more abundant Na^+ ions. This line of reasoning is consistent with our current understanding of NMDARs, which are similarly blocked in a voltage-dependent manner by extracellular Ca^{2+} (see Figs. 7 and 8 in ref. 41) with the added distinction that they are also blocked by Mg^{2+} (refs. 42,43), which permits them to act as coincident detectors at glutamatergic synapses. By extension, we predict that the more abundantly expressed edited AMPARs, which do not transport Ca^{2+}, also exhibit a Ca^{2+} block, not because it plays a significant role in the selective transport of divalent ions, but rather by virtue of possessing an extracellular vestibule (that is, site-G), which is common to all AMPARs.

Ca^{2+} recognition site outside the SF

The SF plays a central role in controlling ion transport in the cation-permeating pore-loop ion channel family with fourfold (pseudo) symmetry[44], which includes potassium channels, calcium channels, sodium channels, cyclic nucleotide-gated channels, iGluRs and TRP channels. In potassium channels, to achieve high selectivity to K^+, the SF maintains an optimal architecture for dehydrated K^+ but deforms into a non-permeating conformation with other cations[14]. By contrast, selectivity for Ca^{2+} in calcium channels is achieved by the negatively charged glutamic acid side chain in the SF that forms a high-affinity Ca^{2+} binding site[26]. The presence of Ca^{2+} in the pore prevents Na^+ from entering, whereas Na^+ permeates efficiently in the absence of Ca^{2+}, exhibiting an anomalous mole-fraction effect[15]. The Ca^{2+} in the SF must be knocked off by a charge repulsion from another Ca^{2+} entering the pore[26]. A similar mechanism is proposed for the Ca^{2+}-selective TRPV6 channel[27]. The cyclic nucleotide-gated channel is non-selective, permeable to both Ca^{2+} and Na^+, but exhibits a Ca^{2+}-mediated channel block[45,46] whose characteristic ion conduction properties are also supported by the mechanism within the SF[47]. By contrast, our observation in CP-AMPARs

https://doi.org/10.1038/s41594-024-01228-3

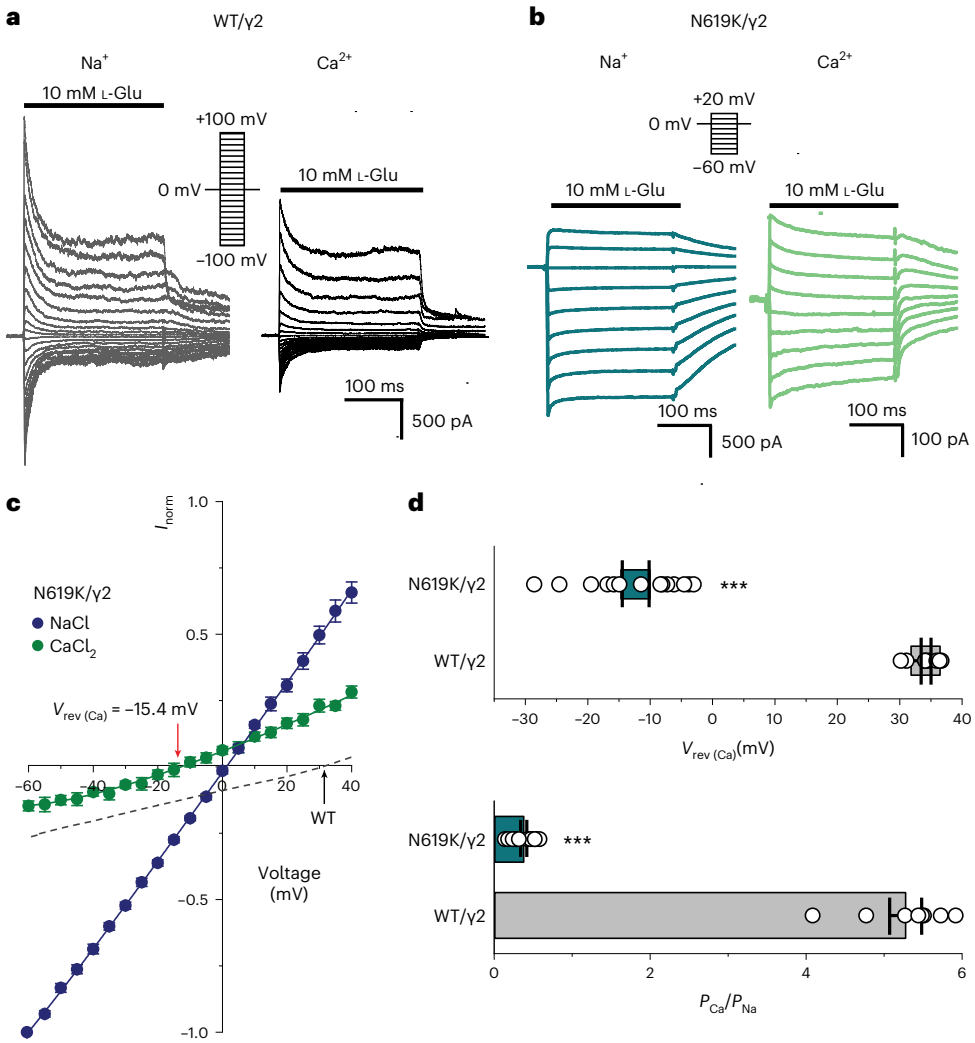

Fig. 6 | Calcium block and permeation are affected by N619K mutation. **a**,**b**, Example traces of responses from WT/γ2 (gray in Na^+, black in Ca^{2+}) and N619K/γ2 (dark cyan in Na^+, green in Ca^{2+}) at various membrane potentials (in 10 mV increments) in the absence of spermine. Receptors were activated with 10 mM L-glutamate. External solutions: Na^+, 150 mM Na^+ recording solution (patch no. 190117p5 for WT/γ2; patch no. 221124p2 for N619K/γ2); and Ca^{2+}, 108 mM Ca^{2+} recording solution (patch no. 190117p5 for WT/γ2 and no. 221124p2 for N619K/γ2). **c**, Current–voltage (*I*–*V*) plots of mutant N619K/γ2 receptors ($n = 10$) in external 150 mM Na^+ (blue circles) or 108 mM Ca^{2+} (green circles). *I*–*V* plot of WT/γ2 receptors ($n = 8$) in 108 mM Ca^{2+} (dashed black line). Data are presented as mean values ± s.e.m. **d**, Top: scatterplot comparing the reversal potential in 108 mM Ca^{2+} from WT/γ2 and N619K/γ2. Gray (WT/γ2) and cyan (N619K/γ2) squares indicate average with s.e.m. ($V_{rev} = 34.1 \pm 0.8$ mV for WT/γ2, $n = 8$; $V_{rev} = -15.4 \pm 2.3$ mV N619K/γ2, $n = 10$; unpaired two-sided *t*-test with Welch correction, $P < 0.001$). Bottom: comparison of the relative divalent permeabilities (P_{Ca2+}/P_{Na+}) of WT/γ2 and mutant N619K/γ2 receptors ($P_{Ca2+}/P_{Na+} = 5.28 \pm 0.21$ for WT/γ2, $n = 8$; $P_{Ca2+}/P_{Na+} = 0.32 \pm 0.04$ for N619K/γ2, $n = 10$) unpaired two-sided *t*-test with Welch correction, $P < 0.001$) (also see Supplementary Table 8).

suggests that efficient Ca^{2+} transport requires the preferential capture of Ca^{2+} at the open gate in the upper pore before Ca^{2+} reaches the SF in the lower pore. We suggest that site-G is a weak Ca^{2+} binding site compared with those found in the SF of Ca^{2+}-selective channels because the surrounding side chains are neutral in site-G, whereas in highly Ca^{2+}-selective channels they are acidic. The Ca^{2+} remains hydrated at site-G but with only four water molecules resolved at the distance (2.4 Å) of a primary hydration shell (Fig. 2l), which is consistent with a weak binding site. Indeed, the hydration of Ca^{2+} at site-G contrasts from the octameric oxygen coordination offered by four carboxylic acidic side chains in the high-affinity Ca^{2+} binding site in the SF of $Ca_V1.1$, $Ca_V3.1$ and TRPV6 (refs. 25,27,48). In the case of Ca_VAb, it is proposed that the high-affinity binding of Ca^{2+} to the SF is mediated indirectly by the hydration shell that consists of eight water molecules[26], which agrees with the idea that coordination of Ca^{2+} by only four water molecules at site-G would form a weaker binding site.

Does site-G have a shared function in the iGluR family?

Given the prevalence of the SYTANLAAF motif in all mammalian iGluR subfamilies, it may be envisaged that site-G fulfills a common role in Ca^{2+} permeation. However, site-G may not convert to a Ca^{2+} binding site in all cases, based on the precedence of de-coupling between gating and Ca^{2+} binding observed in the N619K mutant (Fig. 7). We predict that Ca^{2+} binding to site-G, and thus the coupling, is less efficient in a subset of invertebrate iGluRs that encode lysine at the position equivalent to N619 in rat GluA2 (ref. 49). The efficacy of an open gate converting to an efficient Ca^{2+} binding site may depend on how close the open conformation approaches those that are optimal for Ca^{2+} binding. We suggest that the exact open gate architecture, and by implication, the composition of subunits and dynamics associated with gating, determines whether site-G converts to an efficient Ca^{2+} binding site. In this context, gate-opening and Ca^{2+} binding may not be coupled at site-G in kainate-type iGluRs, given its low divalent permeability. The

https://doi.org/10.1038/s41594-024-01228-3

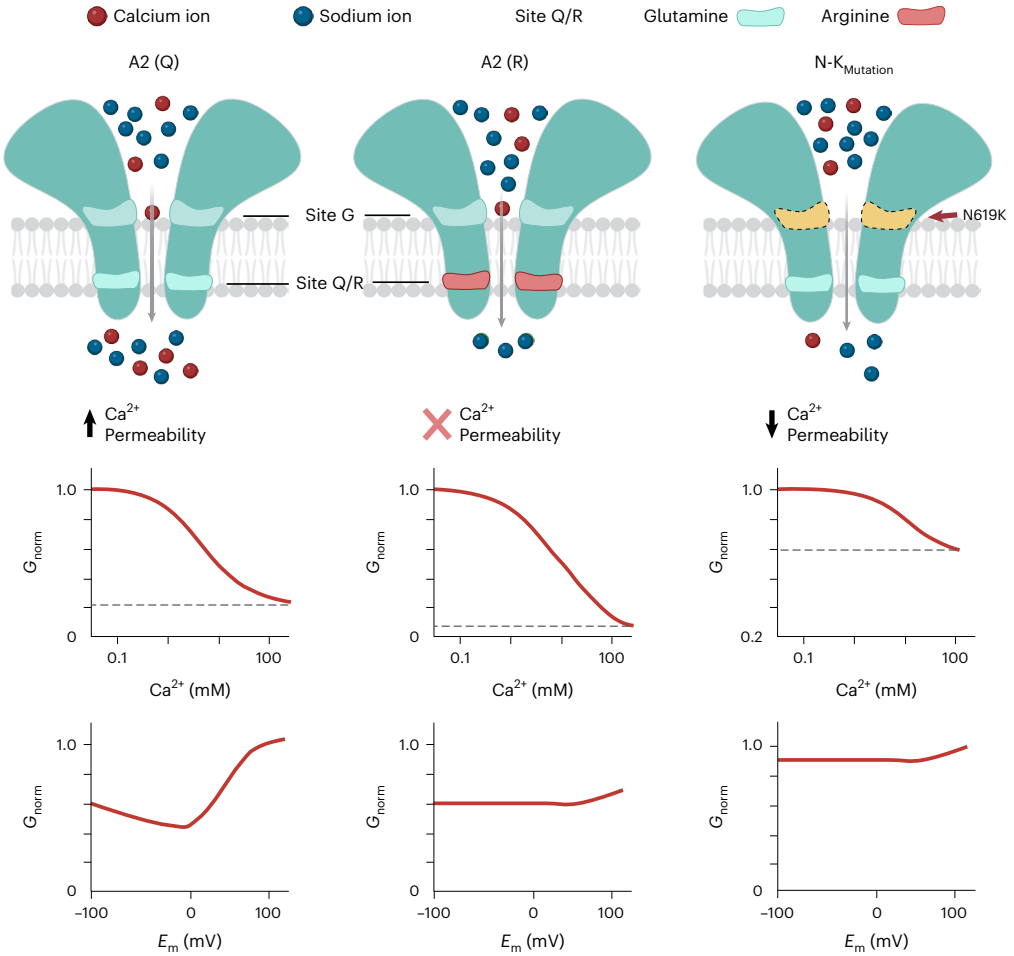

Fig. 7 | Schematic model for the function of site-G. Transport of Ca^{2+} through the AMPAR pore requires both site-G and the Q/R site. Site-G is at the channel gate outside the membrane electric field, and the Q/R site of the SF sits within the membrane electric field. Left: when Ca^{2+} binds to site-G, it partially prevents the passage of Na^+, causing an external Ca^{2+} block of currents carried by Na^+. As a result, Ca^{2+} entry to the Q/R site is maintained even though the physiological external Ca^{2+} concentration is about 50-fold lower than Na^+. This distinction accounts for the efficient divalent permeability in GluA2-iQ (A2(Q)) channels. Middle: in GluA2-iR (A2(R)), Ca^{2+} can still access site-G but cannot permeate beyond the Q/R site. An external Ca^{2+} block is present and is voltage-independent, consistent with site-G being located outside the membrane electric field. Right: for GluA2-iQ N619K mutant channels (N-K mutant), site-G can no longer bind Ca^{2+}, and thus the external Ca^{2+} block is weak. Attenuated site-G reduces the ability of Ca^{2+} to reach the Q/R site, ultimately leading to lower Ca^{2+} permeability.

NMDARs have greater Ca^{2+} permeability than CP-AMPARs, and the gate of both receptors is encoded by the identical amino acid sequence (SYTANLAAF). Thus, given that NMDARs are subject to an external Ca^{2+} block that may be mediated by a Ca^{2+} binding site in the upper pore, as discussed above, it seems natural to presume that the gate of NMDARs would adopt a conformation similar to site-G with efficient Ca^{2+} binding capacity. Taken together, future work is necessary to solve the open state structure of kainate-type iGluRs and examine whether alternative conformations exist for the open gate of NMDARs in addition to those that are currently known[50,51].

In conclusion, we have identified that the gate of the AMPAR contains a transient Ca^{2+} binding site, site-G, that is revealed only in the open state. The evidence for ion recognition and regulation of ion permeation mediated by site-G, outside of the SF, advances our understanding of the nature of divalent cation permeation in AMPARs specifically as well as non-selective cation channels in general.

Online content

Any methods, additional references, Nature Portfolio reporting summaries, source data, extended data, supplementary information, acknowledgements, peer review information; details of author contributions and competing interests; and statements of data and code availability are available at https://doi.org/10.1038/s41594-024-01228-3.

References

1. Hansen, K. B. et al. Structure, function, and pharmacology of glutamate receptor ion channels. *Pharm. Rev.* **73**, 298–487 (2021).
2. Greger, I. H., Watson, J. F. & Cull-Candy, S. G. Structural and functional architecture of AMPA-type glutamate receptors and their auxiliary proteins. *Neuron* **94**, 713–730 (2017).
3. Cull-Candy, S. G. & Farrant, M. Ca^{2+}-permeable AMPA receptors and their auxiliary subunits in synaptic plasticity and disease. *J. Physiol.* **599**, 2655–2671 (2021).
4. Sobolevsky, A. I., Rosconi, M. P. & Gouaux, E. X-ray structure, symmetry and mechanism of an AMPA-subtype glutamate receptor. *Nature* **462**, 745–756 (2009).
5. Nakagawa, T., Cheng, Y., Ramm, E., Sheng, M. & Walz, T. Structure and different conformational states of native AMPA receptor complexes. *Nature* **433**, 545–549 (2005).
6. Meyerson, J. R. et al. Structural mechanism of glutamate receptor activation and desensitization. *Nature* **514**, 328–334 (2014).
7. Armstrong, N. & Gouaux, E. Mechanisms for activation and antagonism of an AMPA-sensitive glutamate receptor: crystal structures of the GluR2 ligand binding core. *Neuron* **28**, 165–181 (2000).

8. Mayer, M. L. et al. The challenge of interpreting glutamate-receptor ion-channel structures. *Biophys. J.* **113**, 2143–2151 (2017).
9. Chen, S. et al. Activation and desensitization mechanism of AMPA receptor–TARP complex by cryo-EM. *Cell* **170**, 1234–1246.e14 (2017).
10. Twomey, E. C., Yelshanskaya, M. V., Grassucci, R. A., Frank, J. & Sobolevsky, A. I. Channel opening and gating mechanism in AMPA-subtype glutamate receptors. *Nature* **549**, 60–65 (2017).
11. Zhang, D., Watson, J. F., Matthews, P. M., Cais, O. & Greger, I. H. Gating and modulation of a hetero-octameric AMPA glutamate receptor. *Nature* **594**, 454–458 (2021).
12. Burnashev, N. et al. Control by asparagine residues of calcium permeability and magnesium blockade in the NMDA receptor. *Science* **257**, 1415–1419 (1992).
13. Brown, P., McGuire, H. & Bowie, D. Stargazin and cornichon-3 relieve polyamine block of AMPA receptors by enhancing blocker permeation. *J. Gen. Physiol.* **150**, 67–82 (2018).
14. Zhou, Y., Morais-Cabral, J. H., Kaufman, A. & MacKinnon, R. Chemistry of ion coordination and hydration revealed by a K^+ channel–Fab complex at 2.0 Å resolution. *Nature* **414**, 43–48 (2001).
15. Hille, B. *Ion Channels of Excitable Membranes* 3rd edn (Sinauer, 2001).
16. Hawken, N. M., Zaika, E. I. & Nakagawa, T. Engineering defined membrane-embedded elements of AMPA receptor induces opposing gating modulation by cornichon 3 and stargazin. *J. Physiol.* **595**, 6517–6539 (2017).
17. Twomey, E. C., Yelshanskaya, M. V., Grassucci, R. A., Frank, J. & Sobolevsky, A. I. Structural bases of desensitization in AMPA receptor–auxiliary subunit complexes. *Neuron* **94**, 569–580.e5 (2017).
18. Dawe, G. B. et al. Distinct structural pathways coordinate the activation of AMPA receptor–auxiliary subunit complexes. *Neuron* **89**, 1264–1276 (2016).
19. Soto, D., Coombs, I. D., Gratacos-Batlle, E., Farrant, M. & Cull-Candy, S. G. Molecular mechanisms contributing to TARP regulation of channel conductance and polyamine block of calcium-permeable AMPA receptors. *J. Neurosci.* **34**, 11673–11683 (2014).
20. Herguedas, B. et al. Mechanisms underlying TARP modulation of the GluA1/2-γ8 AMPA receptor. *Nat. Commun.* **13**, 734 (2022).
21. Harding, M. M. Small revisions to predicted distances around metal sites in proteins. *Acta Crystallogr. D* **62**, 678–682 (2006).
22. Bowie, D., Lange, G. D. & Mayer, M. L. Activity-dependent modulation of glutamate receptors by polyamines. *J. Neurosci.* **18**, 8175–8185 (1998).
23. Kolcheva, M. et al. The pathogenic N650K variant in the GluN1 subunit regulates the trafficking, conductance, and pharmacological properties of NMDA receptors. *Neuropharmacology* **222**, 109297 (2022).
24. Jatzke, C., Hernandez, M. & Wollmuth, L. P. Extracellular vestibule determinants of Ca^{2+} influx in Ca^{2+}-permeable AMPA receptor channels. *J. Physiol.* **549**, 439–452 (2003).
25. Wu, J. et al. Structure of the voltage-gated calcium channel $Ca_v1.1$ at 3.6 Å resolution. *Nature* **537**, 191–196 (2016).
26. Tang, L. et al. Structural basis for Ca^{2+} selectivity of a voltage-gated calcium channel. *Nature* **505**, 56–61 (2014).
27. Saotome, K., Singh, A. K., Yelshanskaya, M. V. & Sobolevsky, A. I. Crystal structure of the epithelial calcium channel TRPV6. *Nature* **534**, 506–511 (2016).
28. Jonas, P. & Burnashev, N. Molecular mechanisms controlling calcium entry through AMPA-type glutamate receptor channels. *Neuron* **15**, 987–990 (1995).
29. Amin, J. B. et al. Two gates mediate NMDA receptor activity and are under subunit-specific regulation. *Nat. Commun.* **14**, 1623 (2023).
30. Amin, J. B., Leng, X., Gochman, A., Zhou, H. X. & Wollmuth, L. P. A conserved glycine harboring disease-associated mutations permits NMDA receptor slow deactivation and high Ca^{2+} permeability. *Nat. Commun.* **9**, 3748 (2018).
31. Watanabe, J., Beck, C., Kuner, T., Premkumar, L. S. & Wollmuth, L. P. DRPEER: a motif in the extracellular vestibule conferring high Ca^{2+} flux rates in NMDA receptor channels. *J. Neurosci.* **22**, 10209–10216 (2002).
32. Schackert, F. K. et al. Mechanism of calcium permeation in a glutamate receptor ion channel. *J. Chem. Inf. Model.* **63**, 1293–1300 (2023).
33. Biedermann, J., Braunbeck, S., Plested, A. J. R. & Sun, H. Nonselective cation permeation in an AMPA-type glutamate receptor. *Proc. Natl Acad. Sci. USA* **118**, e2012843118 (2021).
34. Minniberger, S., Abdolvand, S., Braunbeck, S., Sun, H. & Plested, A. J. R. Asymmetry and ion selectivity properties of bacterial channel NaK mutants derived from ionotropic glutamate receptors. *J. Mol. Biol.* **435**, 167970 (2023).
35. Mesbahi-Vasey, S., Veras, L., Yonkunas, M., Johnson, J. W. & Kurnikova, M. G. All atom NMDA receptor transmembrane domain model development and simulations in lipid bilayers and water. *PLoS ONE* **12**, e0177686 (2017).
36. Sharma, G. & Stevens, C. F. Interactions between two divalent ion binding sites in N-methyl-D-aspartate receptor channels. *Proc. Natl Acad. Sci. USA* **93**, 14170–14175 (1996).
37. Premkumar, L. S. & Auerbach, A. Identification of a high affinity divalent cation binding site near the entrance of the NMDA receptor channel. *Neuron* **16**, 869–880 (1996).
38. Karakas, E. & Furukawa, H. Crystal structure of a heterotetrameric NMDA receptor ion channel. *Science* **344**, 992–997 (2014).
39. Forsberg, M. et al. Ionized calcium in human cerebrospinal fluid and its influence on intrinsic and synaptic excitability of hippocampal pyramidal neurons in the rat. *J. Neurochem.* **149**, 452–470 (2019).
40. Heinemann, U. & Louvel, J. Changes in $[Ca^{2+}]_o$ and $[K^+]_o$ during repetitive electrical stimulation and during pentetrazol induced seizure activity in the sensorimotor cortex of cats. *Pflug. Arch.* **398**, 310–317 (1983).
41. Ascher, P. & Nowak, L. The role of divalent cations in the N-methyl-D-aspartate responses of mouse central neurones in culture. *J. Physiol.* **399**, 247–266 (1988).
42. Nowak, L., Bregestovski, P., Ascher, P., Herbet, A. & Prochiantz, A. Magnesium gates glutamate-activated channels in mouse central neurones. *Nature* **307**, 462–465 (1984).
43. Mayer, M. L., Westbrook, G. L. & Guthrie, P. B. Voltage-dependent block by Mg^{2+} of NMDA responses in spinal cord neurones. *Nature* **309**, 261–263 (1984).
44. Lee, C. H. & MacKinnon, R. Structures of the human HCN1 hyperpolarization-activated channel. *Cell* **168**, 111–120.e11 (2017).
45. Xue, J., Han, Y., Zeng, W. & Jiang, Y. Structural mechanisms of assembly, permeation, gating, and pharmacology of native human rod CNG channel. *Neuron* **110**, 86–95.e5 (2022).
46. Derebe, M. G., Zeng, W., Li, Y., Alam, A. & Jiang, Y. Structural studies of ion permeation and Ca^{2+} blockage of a bacterial channel mimicking the cyclic nucleotide-gated channel pore. *Proc. Natl Acad. Sci. USA* **108**, 592–597 (2011).
47. Zheng, X. et al. Mechanism of ligand activation of a eukaryotic cyclic nucleotide-gated channel. *Nat. Struct. Mol. Biol.* **27**, 625–634 (2020).

48. Zhao, Y. et al. Cryo-EM structures of apo and antagonist-bound human $Ca_v3.1$. *Nature* **576**, 492–497 (2019).
49. Ramos-Vicente, D. et al. Metazoan evolution of glutamate receptors reveals unreported phylogenetic groups and divergent lineage-specific events. *eLife* **7**, e35774 (2018).
50. Chou, T. H., Tajima, N., Romero-Hernandez, A. & Furukawa, H. Structural basis of functional transitions in mammalian NMDA receptors. *Cell* **182**, 357–371.e13 (2020).
51. Wang, H. et al. Gating mechanism and a modulatory niche of human GluN1–GluN2A NMDA receptors. *Neuron* **109**, 2443–2456. e5 (2021).

Methods

Expression and purification

The cDNA construct of the rat GluA2*flip*Q isoform was tagged with a FLAG epitope near its C-terminal, as previously described[52,53]. A rat TARPγ2 (stargazin) KKEE mutant construct was generated as previously described[16] and a 1D4 tag was fused at the C-terminal end. The two cDNAs were cloned into the DualTetON plasmid[54] to generate a plasmid named DualTetON-A2iQFLAG-KKEE1D4, which DOX dependently expresses both proteins simultaneously. The two proteins were co-expressed without using any tether (Extended Data Fig. 1a). A stable TetON HEK cell line was generated by co-transfecting DualTet ON-A2iQFLAG-KKEE1D4 and a plasmid that confers hygromycin (hyg) resistance, using an established method[52–54]. Clones were isolated in the presence of 30 μM NBQX and 120 μg ml^{-1} hyg. Clone no. 53 was chosen based on its growth rate and expression level of the complex, and was adapted to FreeStyle293 media (Gibco/ThermoFisher) in suspension.

The N619K mutation was introduced using site-directed mutagenesis to the WT GluA2*flip*Q construct. The DualTetON-A2iQ(N619K) FLAG-KKEE1D4 plasmid was used to generate a stable cell line (clone no. 8) that co-expresses GluA2*flip*Q(N619K)-FLAG and TARPγ2 (stargazin) KKEE-1D4, DOX dependently. The expression level of the mutant complex was comparable to the WT complex. The biochemical property was indistinguishable from WT, and thus an identical purification protocol was used for both complexes.

Approximately 1.2–2.4 l of near-saturating suspension culture of clone no. 53 (or clone no. 8 in the case of N619K) in FreeStyle293 media supplemented with 30 μM NBQX and 1:500 diluted anti-clumping agent (Gibco/ThermoFisher, cat. no. 0010057DG) was used as a starting material for each experiment. Cells were induced with 7.5 μg ml^{-1} DOX, 1 mM sodium butylate and 1% FCS for 28 h as previously described[53]. The following procedures were conducted on ice or at 4°C. Cells were centrifuged at 931x*g* for 10 min, washed with DPBS once, centrifuged again and the pellet was flash-frozen in liquid nitrogen for storage. Approximately 10–12 ml of the frozen pellet material was resuspended in Resuspend buffer (25 mM Tris-HCl pH 8.0, 150 mM NaCl, 2 mM TCEP, 15 μM NBQX and protease inhibitors: 1 mM PMSF, 10 μg ml^{-1} aprotinin, 0.5 mM benzamidine, 1 μg ml^{-1} pepstatin A, 5 μg ml^{-1} leupeptin), making the final volume 90 ml. Then 10 ml of 10×digi (25 mM Tris-HCl pH 8.0, 150 mM NaCl, 7.5% digitonin) was added and the mixture was nutated at 4°C for 2.5 h to dissolve the membrane. The large debris was removed by low-speed centrifuge (3,000 rpm, 10 min, at 4°C) and its supernatant was ultracentrifuged at 235,400×*g* in a 45Ti rotor (Beckman) for 1 h. The resulting supernatant was incubated in a batch with 1 ml of FLAG M2 agarose beads (Sigma) for 2 h. The beads were collected by centrifugation at 58×*g* for 5 min and transferred into an empty column. The beads were washed with six column volumes of wash buffer (0.03% GDN, 20 mM Tris-HCl pH 8.0, 150 mM NaCl). The proteins were eluted using 6 ml of wash buffer containing 0.5 mg ml^{-1} FLAG peptide. The eluate was concentrated down to 0.55 ml using Ultrafree 100 KDa MWKO ultrafiltration (Millipore). The concentrated sample was ultracentrifuged at 75,325×*g* for 15 min and applied to Superdex200 Increase column (GE Healthcare) equilibrated with GF buffer (for Open-Na260: 0.03% GDN, 20 mM Tris-HCl pH 8.0, 150 mM NaCl; for Open-Na610: 0.03% GDN, 20 mM Tris-HCl pH 8.0, 500 mM NaCl; for Open-CaNaMg, Closed-CaNaMg and Open-CaNaMg(N619K): 0.03% GDN, 20 mM Tris-HCl pH 8.0, 150 mM NaCl, 10 mM $CaCl_2$, 1 mM $MgCl_2$; for Open-Ca150: 0.03% GDN, 20 mM Tris-HCl pH 8.0, 150 mM $CaCl_2$; for Open-Na110 and Open-Ca10: 0.03% GDN, 20 mM Tris-HCl pH 8.0, 140 mM NMDG). Then 1 M NMDG was buffered with HCl to pH 8.0 and used as a stock solution to prepare other buffers. The isocratic elution (0.5 ml per fraction) was conducted at a flow rate 0.5 ml min^{-1} (Extended Data Fig. 1c). The peak fractions were combined and concentrated down to 30 μl using Ultrafree 100 KDa MWKO ultrafiltration. Purity was checked by SDS–PAGE (Extended Data Fig. 1b). To prepare Open-Ca10, a complex prepared in NMDG was mixed with 0.1 M $CaCl_2$ at a 9:1 ratio. The final protein concentration ranged from 7 to 14 mg ml^{-1}.

Grid preparation

To prepare samples in the open states, 0.8 volume of proteins was mixed with 0.1 volume of 3.3 mM CTZ for 30 min and, before freezing, 0.1 volume of 1 M L-glutamate (pH 7.4) was added. The 1 M L-glutamate solution contains 1.1 M NaOH; therefore, the final concentration of Na^+ increases by 110 mM after adding the agonist to the purified receptors. To prepare samples in the closed state, 0.8 volume of proteins was mixed with 0.1 volume of 3.3 mM CTZ and 0.1 volume of 1 mM CNQX disodium salt (Tocris) and incubated for 15 min before freezing.

A total of 2 μl of protein solution was applied to Quantifoil1.2/1.3 (300 mesh, Cu grid, holy carbon membrane) and plunged into liquid ethane using a Vitrobot Mark4 (ThermoFisher). The standard parameters were blot force = 12, blot time = 4.5 s, temp = 4°C, humidity = 100%, wait time = 30 s and drain time = none. The samples containing 140 mM NMDG or greater than 500 mM NaCl were more viscous than the others, so the filter papers were doubled and blot time was extended to ~6–7 s. Optimal freezing conditions were determined by inspecting the grids using TF20 (FEI/ThermoFisher) or Glacios (ThermoFisher).

Cryo-EM imaging

All data were collected using TitanKriosG4i (ThermoFisher) equipped with BioQuantumK3 detector at Vanderbilt University cryo-EM facility. Images were collected at 50 frames per movie. The aberration-free image shift function was used in EPU (ThermoFisher) semi-automated data collection software. The microscope is equipped with fringe-free optics, which enables a smaller beam diameter for imaging. Objective aperture was not used. Data collection was completed from one grid in a single imaging session that lasted 3.5–5 days. The detector dose rate was at 15.3–15.7 e^- per pixel per second (measured over ice). The total dose was at 50–56 $e^-/Å^2$ (measured over vacuum). Each movie contained 50 frames. At ×105,000 magnification, two shots per hole were taken. At ×130,000 magnification, three to four shots per hole were taken. A representative raw motion-corrected micrograph of Open-Na260 is shown in Extended Data Fig. 1d. Detailed parameters used for data collection in each sample are summarized in Table 1 and Supplementary Table 1.

Common image processing pipeline

The image processing of each dataset follows a common pipeline. Minor modifications were made when necessary. All image processing in the current work was done using Relion3 (ref. 55). Each raw movie stack (50 frames) was motion-corrected (at 4 × 4 patches) and dose-weighted using Motioncorr2 (ref. 56). CTFFIND4 was used to estimate contrast transfer function (CTF) from non-dose-weighted images using 1,024 × 1,024 pixel tiles[57]. All datasets produced excellent statistics in rlnCtfMaxResolution and rlnCtfFigureOfMerit. C2 symmetry was imposed only at the last step of 3D refinement. The NTD, which is flexible relative to the rest of the architecture[5], was included in the 2D and initial 3D classification but was outside the mask used for the focused classification and refinement in 3D. EMD-2680 was used as the initial model. The LBD adopted multiple conformations in all datasets except for the Open-Ca150, which was noticeable as ill-defined LBDs when the particles were aligned using the mask containing LBD-TMD and TARPγ2(KKEE). The alignment was guided towards improving the resolution of the membrane-embedded region at the cost of degrading the alignment of the LBD because the former contains many bundles of alpha helices that generate strong signals. The heterogeneity of LBD conformations was resolved by further focused classification and refinement, imposing C2 symmetry and using the LBD mask, which contains the LBD gating ring (the tetrameric assembly of the LBD). The particles contained in the final refinement of the TMD-STG were

used as input to the LBD classification. The differences between the LBD conformations were characterized as translation and rotation between the two LBD dimers (Extended Data Fig. 5), which were small conformational differences in the organization of the LBDs in the gating ring[9]. When necessary, the composite maps made of the LBD map plus the TMD-STG map were generated using EMDA[58]. The local resolution of the map was estimated using Relion3 and ResMap[59]. The overall resolutions of the maps were estimated by an FSC = 0.143 cutoff in Relion[60] (Extended Data Fig. 2). The image processing and model statistics are summarized in Table 1 and Supplementary Table 1. Angular distributions of assigned angles were inspected to ensure the coverage of the Fourier space. Visual inspection of the map showed no signs of artefacts.

Image processing of Open-Na260

The workflow is summarized graphically in Extended Data Fig. 1f, which follows the general procedure described above. A total of 5,409,247 particles were selected using Autopick, with templates obtained from 2D class averages generated from manually picked ~3,000 particles. Particles were extracted at a box size of 360 pixels and reduced to 64 pixels. The extracted particles were divided into four subsets. Each subset was subjected to 2D classification, specifying 160 classes (Extended Data Fig. 1e). After two rounds of 2D classification, 2,110,000 particles contributed to generating well-defined class averages that contained features of AMPARs and were subjected to further 3D classification. For 3D classification, particles were re-extracted at a box size of 360 pixels and reduced to 180 pixels, resulting in a binning factor of two. Particles were classified into six classes without a mask and without imposing symmetry (C1) for 40 iterations. An additional 20 iterations were conducted by applying a mask covering the LBD and TMD (LBD-TMD) with a regularization parameter at $T = 15$. Three well-defined classes (classes 3, 4 and 6) were selected, totaling 1,240,685 particles (Extended Data Fig. 1f1).

The particles combined from the three classes were re-extracted at a box size of 360 pixels without binning. After CTF refinement, Refine3D and PostProcess were conducted again, followed by Bayesian polishing. Shiny particles were subjected to a second round of CTF refinement. Duplicate particles were removed, and a total of 1,093,405 particles proceeded to the final Refne3D. Refinement and PostProcess were first conducted with C1 (no symmetry) using the TMD-STG mask, which covers the TMD of GluA2 and TARPγ2(KKEE), generating a map with an overall resolution of 2.38 Å. the LBD-TMD mask was also used to generate a 2.50 Å overall resolution map, whose LBDs were ill-resolved owing to conformational heterogeneity. The final refinement, Refine3D and PostProcess were done, imposing C2 symmetry and using the TMD-STG mask, resulting in a map with an overall resolution of 2.29 Å. The angular distributions of the assigned angles show that the side views were the most abundant (Extended Data Fig. 1f2).

To resolve the heterogeneity of the LBDs, the particles were classified into four classes ($T = 50$) using a mask that covers the LBD gating ring (LBD mask) (Extended Data Fig. 1f3). Three of those classes (class 1, 2 and 4, which will be referred to as conf1, conf2 and conf3, respectively) produced well-defined maps at greater than 3.5 Å resolution. The remaining class was ill-defined, indicating substantial heterogeneity of conformations. The LBDs of conf1, conf2 and conf3 were subjected to Refine3D and PostProcess, producing maps with overall resolutions of 3.01 Å, 3.43 Å and 3.04 Å, respectively (Extended Data Fig. 1f4). The angular distributions of the assigned angles were very similar in L1–L3 and consistent with the distribution of the consensus reconstruction described above, indicating that the classification of the LBD is based on conformation rather than angular distribution.

The 3D classification and refinement from the binned images (box size = 180 pixels) resulted in a 4.4 Å map containing the NTD. The tetrameric NTD, organized in dimer-of-dimers, was positioned in the asymmetric orientation relative to the rest of the particle as described previously[53], and no classes adopted a pseudo-symmetric orientation. Atomic models of the LBD, TMD and TARPγ2(KKEE) generated below and the GluA2-NTD (PDB 6U6I) were rigid-body fit into the 4.4 Å map to generate Fig. 1b.

Image processing of Open-CaNaMg

The common pipeline was followed with minor modifications during the first 3D classification. Motion correction and CTF estimation were done as described above. A total of ~5,000,000 particles were selected using Autopick, with templates obtained from 2D class averages generated from manually picking ~3,000 particles. Particles were extracted at a box size of 456 pixels and reduced to 64 pixels. The extracted particles were divided into four subsets. Each subset was subjected to 2D classification, specifying 160 classes. After two rounds of 2D classification, ~1,200,000 particles contributed to generating well-defined class averages and were subjected to further 3D classification. For 3D classification, particles were re-extracted at a box size of 456 pixels and then reduced to 180 pixels. Particles were classified into six classes without a mask and without imposing symmetry for 37 iterations with a regularization parameter at $T = 6$. Four well-defined classes (class 2 = 235,679 particles; class 3 = 217,442 particles; class 5 = 130,488 particles; class 4 = 238,429 particles) were selected, totaling 822,038 particles. The particles were re-extracted at 456 pixels and rescaled to 360 pixels, which resulted in apix = 0.819 Å per pixel, equivalent to the apix in Open-Na260. Refine3D and PostProcess using the TMD-STG mask resulted in a reconstruction of an overall resolution of 2.61 Å. After CTF refinement, Refine3D and PostProcess were conducted again, producing a 2.63 Å map (the resolution was reduced but the map quality improved). The particles were subjected to Bayesian polishing, with training followed by polishing. Refine3D and PostProcess produced a map at an overall resolution of 2.59 Å. The LBD-TMD mask was also used to generate a 2.63 Å overall resolution map, whose LBDs were ill-resolved owing to conformational heterogeneity. The final refinement, Refine3D and PostProcess were done, imposing C2 symmetry and using the TMD-STG mask, producing a map with an overall resolution of 2.44 Å.

To resolve the heterogeneity of the LBDs, the particles were classified into four classes ($T = 50$) using the LBD mask for 40 iterations. Two classes (class 2 = 204,515 particles and class 3 = 210,811 particles, which will be referred to as conf1 and conf2, respectively) produced a well-defined map at 3.5 Å resolution. The remaining class was ill-defined, indicating substantial heterogeneity of conformations. The LBDs of conf1 and conf2 were subjected to Refine3D and PostProcess, producing maps with overall resolutions of 2.78 Å and 3.14 Å, respectively.

Image processing of Open-Na610

The common pipeline was followed with minor modifications during the first 3D classification. Motion correction and CTF estimation were done as described. About 5,100,000 particles were selected using Autopick with templates used for Open-Na150. Particles were extracted at a box size of 360 pixels and reduced to 64 pixels. The extracted particles were divided into four subsets, and each subset was subjected to 2D classification, specifying 160 classes. Well-defined classes selected during the first round were re-extracted and rescaled to a box size of 180 pixels. After the second round of 2D classification, ~2,285,000 particles contributed to generating well-defined class averages and were subjected to further 3D classification. For 3D classification, particles were re-extracted at a box size of 456 pixels and reduced to 180 pixels. Particles were classified into six classes without a mask and without imposing symmetry for 36 iterations with a regularization parameter at $T = 4$. Then, the classification was continued up to 60 iterations using the LBD-TMD mask with $T = 15$. Three well-defined classes (class 1 = 244,459 particles; class 3 = 300,808 particles; class 4 = 355,887 particles) were selected, totaling 901,154 particles. The particles were

re-extracted at a box size of 360 pixels without rescaling. Refine3D and PostProcess using the LBD-TMD mask were conducted (C1) for 21 iterations, generating a reconstruction with an overall resolution of 2.79 Å. The focused refinement was then continued from iteration 19 using the TMD-STG mask, generating a reconstruction with an overall resolution of 2.59 Å. After CTF refinement, Refine3D and PostProcess were conducted (C1) again in two steps using both masks, producing maps with overall resolutions of 2.66 Å and 2.61 Å with the LBD-TMD mask and TMD-STG mask, respectively. The resolution was reduced but map quality improved with CtfRefine. The particles were subjected to Bayesian polishing, with training followed by polishing. The Refine3D and PostProcess produced C1 maps with overall resolutions of 2.57 Å and 2.50 Å, using the LBD-TMD mask and TMD-STG mask, respectively. In the map generated using the LBD-TMD mask, the LBDs were ill-resolved owing to conformational heterogeneity. The final focused refinement, Refine3D and PostProcess were done, imposing C2 symmetry in two steps using both the LBD-TMD mask and TMD-STG mask, resulting in maps with overall resolutions of 2.46 Å and 2.40 Å, respectively.

To resolve the heterogeneity of the LBDs, the particles were classified, imposing C2 symmetry, into four classes ($T = 50$) using the LBD mask for 40 iterations. Three classes (class 1 = 207,914 particles; class 2 = 220,191 particles; class 4 = 299,853 particles, which will be referred to as conf1, conf2 and conf3, respectively) produced well-defined maps at 3.5 Å resolution. The remaining class was ill-defined, indicating substantial heterogeneity of conformations. The LBDs of conf1, conf2 and conf3 were subjected to Refine3D and PostProcess, producing maps with overall resolutions of 3.08 Å, 2.98 Å and 3.01 Å, respectively.

Image processing of Open-Ca150

The common pipeline was followed with minor modifications during the first 3D classification. Motion correction and CTF estimation were done as described above. Approximately ~5,573,000 particles were selected using Autopick with templates used in Open-CaNaMg. Particles were extracted at a box size of 456 pixels and reduced to 64 pixels. The extracted particles were divided into four subsets. Each subset was subjected to 2D classification, specifying 160 classes. After 2D classification, ~1,640,000 particles contributed to generating well-defined class averages and were subjected to further 3D classification. For 3D classification, particles were re-extracted at a box size of 456 pixels and reduced to 180 pixels. Particles were classified into three classes without a mask and without imposing symmetry for 40 iterations, with a regularization parameter at $T = 4$. Then the classification was continued up to 60 iterations using the LBD-TMD mask with $T = 15$. The well-defined class 1, containing 540,796 particles, was selected. The particles were re-extracted at 456 pixels and rescaled to 360 pixels, which resulted in apix = 0.819 Å per pixel, equivalent to the apix in Open-Na260. Refine3D and PostProcess using the LBD-TMD mask were conducted (C1) and converged in 24 iterations, generating a reconstruction with an overall resolution of 3.04 Å. The focused refinement was then continued from iteration 13 using the TMD-STG mask, generating a reconstruction with an overall resolution of 2.86 Å. After CTF refinement, Refine3D and PostProcess were conducted (C1) again in two steps using both masks, producing maps with overall resolutions of 2.95 Å and 2.84 Å with the LBD-TMD mask and TMD-STG mask, respectively. The particles were subjected to Bayesian polishing, with training followed by polishing. The Refine3D and PostProcess produced C1 maps of overall resolutions of 2.84 Å and 2.78 Å, using the LBD-TMD mask and TMD-STG mask, respectively. In the map generated using the LBD-TMD mask, the LBDs were ill-defined. The final focused refinement, Refine3D and PostProcess were done, imposing C2 symmetry in two steps using both the LBD-TMD mask and TMD-STG mask, resulting in maps with overall resolutions of 2.73 Å and 2.58 Å, respectively. The overall yield of particles and resolution was lower than the other dataset, possibly owing to stronger beam-induced motion that may have been caused by using the 150 mM $CaCl_2$.

To resolve the heterogeneity of the LBDs, the particles were classified, imposing C2 symmetry, into three classes ($T = 50$), using the LBD mask for 40 iterations. One of the classes (class 3 = 192,490 particles) produced a well-defined map at 3.5 Å resolution. The remaining class was ill-defined, indicating substantial heterogeneity of conformations. Refine3D and PostProcess produced maps with overall resolutions of 3.14 Å.

Image processing of Open-Na110

The common pipeline was followed with minor modifications during the first 3D classification. Motion correction and CTF estimation were done as described above. Then ~8,603,000 particles were selected using Autopick with templates used in Open-CaNaMg. Particles were extracted at a box size of 456 pixels and reduced to 64 pixels. The extracted particles were divided into six subsets. Each subset was subjected to 2D classification, specifying 160 classes. After two rounds of 2D classification, ~2,892,000 particles contributed to generating well-defined class averages and were subjected to further 3D classification. For 3D classification, particles were extracted at a box size of 456 pixels and reduced to 180 pixels, and then classified into three classes without a mask and without imposing symmetry (C1) for 18 iterations with a regularization parameter at $T = 4$. The classification continued with the LBD-TMD mask up to 40 iterations with $T = 20$. One well-defined class was selected, totaling 692,680 particles. The particles were re-extracted at 456 pixels and rescaled to 360 pixels, which resulted in apix = 0.819 Å per pixel, equivalent to the apix in Open-Na260. Refine3D and PostProcess using the LBD-TMD mask and TMD-STG mask resulted in C1 maps with overall resolutions of 2.59 Å and 2.46 Å, respectively. After CTF refinement, Refine3D and PostProcess were conducted (C1) again in two steps using both masks, producing maps with overall resolutions of 2.59 Å and 2.52 Å with the LBD-TMD mask and TMD-STG mask, respectively. The particles were subjected to Bayesian polishing, with training followed by polishing. The Refine3D and PostProcess produced C1 maps with overall resolutions of 2.46 Å and 2.42 Å, using the LBD-TMD mask and TMD-STG mask, respectively. In the map generated using the LBD-TMD mask, the LBDs were ill-defined. The final focused refinement, Refine3D and PostProcess were done, imposing C2 symmetry in two steps using both the LBD-TMD mask and TMD-STG mask, resulting in maps with overall resolutions of 2.38 Å and 2.34 Å, respectively.

To resolve the heterogeneity of the LBDs, the particles were classified into three classes ($T = 50$) using the LBD mask for 40 iterations. Two classes (class 2 = 189,181 particles; class 3 = 218,818 particles, which will be referred to as conf1 and conf2, respectively) produced a well-defined map at 3.5 Å resolution. The remaining class was ill-defined, indicating substantial heterogeneity of conformations. The LBDs of conf1 and conf2 were subjected to Refine3D and PostProcess, producing maps with overall resolutions of 3.11 Å and 3.35 Å, respectively.

Image processing of Open-Ca10

The common pipeline was followed with minor modifications during the first 3D classification. Motion correction and CTF estimation were done as described above. Then, ~7,059,000 particles were selected using Autopick with templates used in Open-CaNaMg. Particles were extracted at a box size of 456 pixels and reduced to 64 pixels. The extracted particles were divided into four subsets. Each subset was subjected to 2D classification, specifying 160 classes. After two rounds of 2D classification, ~1,952,000 particles contributed to generating well-defined class averages that contain features of AMPARs and were subjected to further 3D classification. For 3D classification, particles were extracted at a box size of 456 pixels and reduced to 180 pixels, and classified into three classes without a mask and without imposing symmetry (C1) for 31 iterations with a regularization parameter at $T = 4$. The classification continued with the LBD-TMD mask up to 50 iterations with $T = 20$. One well-defined class was selected, totaling 986,075

particles. The particles were re-extracted at 456 pixels and rescaled to 360 pixels, which resulted in apix = 0.819 Å per pixel, equivalent to the apix in Open-Na260. Refine3D and PostProcess using the LBD-TMD mask and TMD-STG mask resulted in C1 maps with overall resolutions of 2.56 Å and 2.46 Å, respectively. After CTF refinement, Refine3D and PostProcess were conducted (C1) again in two steps using both masks, producing maps of overall resolutions of 2.59 Å and 2.56 Å with the LBD-TMD mask and TMD-STG mask, respectively. The particles were subjected to Bayesian polishing, with training followed by polishing. The Refine3D and PostProcess produced C1 maps of overall resolutions of 2.52 Å and 2.48 Å, using the LBD-TMD mask and TMD-STG mask, respectively. In the map generated using the LBD-TMD mask, the LBDs were ill-defined. The final focused refinement, Refine3D and PostProcess were done, imposing C2 symmetry in two steps using both the LBD-TMD mask and TMD-STG mask, resulting in maps with overall resolutions of 2.44 Å and 2.36 Å, respectively.

To resolve the heterogeneity of the LBDs, the particles were classified into four classes ($T = 50$) using the LBD mask for 40 iterations. Two classes (class 1 = 215,389 particles; class 2 = 278,786 particles, which will be referred to as conf1 and conf2, respectively) produced a well-defined map at 3.5 Å resolution. The remaining class was ill-defined, indicating substantial heterogeneity of conformations. The LBDs of conf1 and conf2 were subjected to Refine3D and PostProcess, producing maps with overall resolutions of 3.01 Å and 3.14 Å, respectively.

Image processing of Open-CaNaMg/N619K

The common pipeline was followed with minor modifications during the first 3D classification. Motion correction and CTF estimation were done as described above. 2D class averages were generated from 109,101 particles that were selected using Autopick with the template used in Open-CaNaMg. A subset of well-defined class averages was further used as templates to select ~7,006,000 particles using Autopick from all micrographs. Particles were extracted at a box size of 456 pixels and reduced to 64 pixels. The extracted particles were divided into five subsets. Each subset was subject to 2D classification, specifying 160 classes. After two rounds of 2D classification, ~1,957,000 particles contributed to generating well-defined class averages and were subjected to further 3D classification. For 3D classification, particles were re-extracted at a box size of 456 pixels and reduced to 180 pixels. Particles were classified into six classes without a mask and without imposing symmetry (C1) for 40 iterations with a regularization parameter at $T = 4$. The classification continued with the LBD-TMD mask up to 60 iterations with $T = 15$. Two well-defined classes (class 1 = 357,587 particles; class 5 = 336,348 particles) were selected, totaling 693,935 particles. The particles were re-extracted at 456 pixels and rescaled to 360 pixels, which resulted in apix = 0.819 Å per pixel, equivalent to the apix in Open-Na260. Refine3D and PostProcess using the LBD-TMD mask and TMD-STG mask resulted in C1 maps of overall resolutions of 2.61 Å and 2.44 Å, respectively. After CTF refinement, Refine3D and PostProcess were conducted (C1) using the TMD-STG mask, producing a map with an overall resolution of 2.61 Å. The particles were subjected to Bayesian polishing, first the training and then the actual polishing. The Refine3D and PostProcess produced C1 maps of overall resolutions of 2.59 Å and 2.50 Å, using the LBD-TMD mask and TMD-STG mask, respectively. In the map generated using the LBD-TMD mask, the LBDs were ill-defined. The final focused refinement, Refine3D and PostProcess were done, imposing C2 symmetry in two steps using both the LBD-TMD mask and TMD-STG mask, resulting in maps with overall resolutions of 2.48 Å and 2.38 Å, respectively.

To resolve the heterogeneity of the LBDs, the particles were classified into four classes ($T = 50$) using a mask that covers the LBD gating ring (LBD mask) for 40 iterations. Two classes (class 1 = 203,784 particles; class 3 = 210,604 particles, which will be referred to as conf1 and conf2, respectively) produced well-defined maps at 3.5 Å resolution. The remaining class was ill-defined, indicating substantial heterogeneity of conformations. The LBDs of conf1 and conf2 were subjected to Refine3D and PostProcess, producing maps with overall resolutions of 3.14 Å and 3.17 Å, respectively.

Image processing of Closed-CaNaMg

The common pipeline was followed with minor modifications during the first 2D and 3D classification. The data processing was initiated for the first 14,999 micrographs when it became available during the session after the first 2 days of data collection. The remaining 19,554 micrographs were processed upon completion of the entire session. As described above, the entire dataset is derived from a single grid, and thus splitting the data into two batches is done to initiate data processing sooner and to evaluate whether prolonged imaging of the identical grid would cause any deterioration to the image quality. Image quality was not affected, as described in the following section. Motion correction and CTF estimation were done as described for Open-Na260. A total of ~3,900,000 particles (batch 1) and ~4,600,00 particles (batch 2) were selected using Autopick. Particles were extracted at a box size of 456 pixels and reduced to 64 pixels. The extracted particles were subjected to 2D classification, resulting in ~1,020,000 particles (batch 1) and ~1,007,00 particles (batch 2) contributing to the generation of well-defined class averages that contain features of AMPARs. Each batch was subjected to identical 3D classification, refinement and PostProcess separately and produced maps of the TMD-STG with similar overall resolutions of 2.66 Å (batch 1) and 2.56 Å (batch 2).

Particles of two batches after 2D classification were combined (~2,027,000 particles) and re-extracted at a box size of 456 pixels and then rescaled to 180 pixels. Particles were classified into six classes without a mask and without imposing symmetry (C1) for 40 iterations with a regularization parameter at $T = 6$. Two well-defined classes (class 3 = 484,918 particles; class 4 = 362,460 particles) were selected, totaling 847,378 particles. The particles were re-extracted at 456 pixels and rescaled to 360 pixels, which resulted in apix = 0.819 Å per pixel, equivalent to the apix in Open-Na260. Refine3D and PostProcess using the STG-TMD mask resulted in a C1 map with an overall resolution of 2.57 Å. After CTF refinement, Refine3D and PostProcess were conducted (C1) using the TMD-STG mask, producing a map with an overall resolution of 2.59 Å. The particles were subjected to Bayesian polishing, with training followed by polishing. The Refine3D and PostProcess produced C1 maps of overall resolutions of 2.52 Å and 2.42 Å, using the LBD-TMD mask and TMD-STG mask, respectively. In the map generated using the LBD-TMD mask, the LBDs were ill-defined. The final focused refinement, Refine3D and PostProcess were done, imposing C2 symmetry using the TMD-STG mask, resulting in a map with an overall resolution of 2.32 Å.

The heterogeneity of the LBDs was resolved by classifying the particles into four classes ($T = 50$) using the LBD mask for 40 iterations. Two classes (class 1 = 215,404 particles; class 3 = 262,250 particles, which will be referred to as conf1 and conf2, respectively) produced well-defined maps at 3.5 Å resolution. The remaining class was ill-defined, indicating substantial heterogeneity of conformations. The LBDs of conf1 and conf2 were subjected to Refine3D and PostProcess, producing maps with overall resolutions of 2.76 Å and 2.81 Å, respectively.

Modeling

The reference model, PDB 5WEO5weo, was divided into domains and rigid-body fit into the EM density map using Chimera (v1.14)[61]. The fit was further adjusted using the jiggle fit function in Coot (v0.9.8.7)[62]. Further manual adjustment with the real space refine zone function in Coot was used to generate an atomic model. H_2O was modeled manually to densities that are within hydrogen bond distance to potential acceptors and donors. The pore-occupying densities in the Open-Na110 (that is, containing 140 mM $NMDG^+$ and 110 mM Na^+) were all interpreted to be water. Although some may have been Na^+ ions, we did not have sufficient experimental basis to assign them as ions. In addition,

none of the densities were large enough to accommodate NMDG. The Open-Na110 provided the reference to find water molecules in other structures. In fact, many water molecules were found within a distance of 1.2 Å from where they were found in the Open-Na110 (for example, see Extended Data Fig. 8). In addition, the knowledge of their average intermolecular distance (2.8 Å) and average neighbors (4.4) were used when a network of H_2O was observed[15]. Validation was conducted using Coot. The generated model was further refined using the real_space_refine tool in Phenix (v1.18-1.20)[63]. Real-space refinement was conducted by imposing secondary structure restrains by annotating helices and sheets in the PBD file. To prevent overfitting of the models into the density, refinement was run for five cycles with strict geometric restraints of 0.005–0.01 for bond length and 0.5–1 for bond angle, while non-crystallographic symmetry, consistent with C2 symmetry of the map, was imposed when necessary. With the default restraints library provided by real_space_refine, the distances between Ca^{2+} and the nearest water were in the range of 2.5–2.6 Å. The refinement outcome was virtually identical when custom geometry restraints of a target distance of 2.39 ± 0.1 Å were imposed[21], which resulted in a 2.4 Å spacing between Ca^{2+} and the nearest water. Ca^{2+} was modeled and refined without conflict at site-G in Open-Ca10, Open-CaNaMg and Open-Ca150. In addition, model refinement was successful when Ca^{2+} was placed at site-Q586/7 in Open-Ca150. The FCS of the model versus map was output by Mtriage. Cryo-EM validation tools MolProbity and Mtriage were used for validation (Table 1 and Supplementary Table 1). The maps containing both the LBD and the TMD-STG were interpreted by rigid-body fitting the atomic models of individual fragments. To interpret the connection between the fragments, composite maps were used. Pymol (Schrödinger) and Chimera[61] were used to further analyze the structure and generate figures. The pore radius accessible to solvent was estimated using CHAP software[64].

Multiple sequence alignment

Clustal Omega[65] was used to align the iGluR sequences from various species.

Cell culture and transfection for electrophysiology

HEK293T-TetON cells were maintained in DMEM high glucose containing glutamine and without sodium pyruvate. The media was supplemented with 10% FBS (Gibco) and 1% penicillin and streptomycin stock solution (Gibco; 10,000 U ml^{-1} of penicillin and 10,000 µg ml^{-1} of streptomycin). Cells were plated at low density (1.6×10^4 cells per ml) on poly-D-lysine-coated, 35 mm plastic dishes and were transiently transfected 48 h later using the calcium phosphate technique, as previously described[66]. To promote the synthesis of GluA2(Q)-γ2, GluA2(R)-γ2, $GluA2(Q)_{(N619K)}$-γ2, all flip isoforms, encoded in the plasmids, and doxycycline was added approximately 24 h before performing experiments at a final concentration of 2 µg ml^{-1}.

Electrophysiology

Experiments were performed 24 h after adding doxycycline to transfected cells. Agonist or antagonist solutions were rapidly applied to outside-out patches excised from transfected cells using a piezoelectric stack (Physik Instrumente). Solution exchange (10–90% rise time of 250–350 µs) was determined by measuring the liquid junction current at the end of an experiment. All recordings were performed using an Axopatch 200B (Molecular Devices) with thick-walled, borosilicate glass pipettes (3–6 MΩ) coated with dental wax to reduce electrical noise. Series resistance (3–12 MΩ) was compensated by 95%. To study calcium block in AMPA receptors, voltage ramps were recorded at a range of holding potentials from −100 mV to +100 mV. Data acquisition was performed using pClamp10 software (Molecular Devices) and was tabulated using Excel (Microsoft). All experiments were performed at room temperature (20–22 °C).

All chemicals were purchased from Sigma-Aldrich unless otherwise indicated. The external solution contained (in mM) 150 NaCl, 5 HEPES and 0.1 $CaCl_2$, at pH 7.3–7.4. The internal solution contained (in mM) 115 NaCl, 10 NaF, 5 HEPES, 5 Na_4BAPTA (Life Technologies), 1 $MgCl_2$, 0.5 $CaCl_2$ and 10 Na_2ATP, pH 7.3–7.4. The osmotic pressure of all solutions was adjusted to 295–300 mOsm with sucrose, if necessary. For polyamine block experiments, instead of 10 mM Na_2ATP, 30 µM spermine was included in the internal solution. For calcium block experiments, external Ca^{2+} was added into 150 mM NaCl to give a final concentration of either 0.3, 1, 2, 5, 10, 20 or 30 mM, except for the highest (108 mM) Ca^{2+} solution, which contained only 108 mM $CaCl_2$ (+HEPES) with no added NaCl. In all cases, cyclothiazide was added at a final concentration of 100 µM to the control and agonist external solutions to reduce receptor desensitization. Currents recorded in the control solution were used to leak-subtract experimental records. For the calcium permeation experiments (Fig. 6), high-concentration external Ca^{2+} contained (in mM) 108 $CaCl_2$ and 5 HEPES (in mM) at pH 7.3–7.4 (pH adjusted with Ca $(OH)_2$).

Concentrated (10×) agonist stock solutions were prepared by dissolving L-glutamate in the appropriate external solution and adjusting the pH to 7.3–7.4; these solutions were stored frozen at −20 °C. Stocks were thawed on the day of the experiment and used to prepare agonist-containing external solutions.

Single permeant blocker model for external Ca^{2+} and internal polyamines

Conductance–voltage (G–V) relationships of the block by external Ca^{2+} or internal polyamines were fit using Origin Pro 2020 (OriginLab) with the following equation from a previous publication[22]:

$$G = \frac{G_{max}}{1 + \frac{[blocker]}{K_d}} \quad (1)$$

where K_d is the dissociation constant at 0 mV and it is defined as:

$$K_d = \frac{k_{off} + k_{perm}}{k_{on}} = \frac{\text{sum of exit rates}}{\text{binding rate}} \quad (2)$$

and redefined as shown:

$$K_d = g \exp\left(\frac{V}{h}\right) + L \exp\left(\frac{V}{k}\right) \quad (3)$$

here, h and k represent the voltage dependence of g (k_{off}/k_{on}) and L (k_{perm}/k_{on}), respectively.

Calcium permeability

I–V relationships were used to calculate reversal potentials in 150 mM external Na^+ and in 108 mM external Ca^{2+} solutions. Fittings were calculated with a polynomial function with an order of four. The x intercept of the polynomial fit was determined to be the reversal potential (V_{rev}). The ratio of Ca^{2+} permeability relative to Na^+ (P_{Ca}/P_{Na}) was calculated by the equation:

$$\frac{P_{Ca}}{P_{Na}} = \frac{[Na^+]_i \left(1 + e^{\frac{V_{rev(Ca)} \times F}{RT}}\right)}{4\left[Ca^{2+}\right]_o \left(e^{\frac{(V_{rev(Ca)} - V_{rev(Na)}) \times F}{RT}}\right)} \quad (4)$$

where P_{Ca} and P_{Na} are the permeability coefficients for Ca^{2+} and Na^+, respectively; F is Faraday's constant; R is the gas constant; and T is the temperature in kelvin.

Kinetics

The gating properties of AMPA receptors were assessed by applying a single voltage ramp (40 ms) from 0 mV to −100 mV to assess the leak current, followed by a 250 ms application of L-glutamate (10 mM) to measure the steady-state equilibrium of agonist-induced receptor

desensitization and the time constant of deactivation (indicated as off kinetics in Fig. 5). Off kinetics (τ_{off}) were fit using a mono-exponential or bi-exponential function as described previously[67] and are presented as weighted means.

Inhibition plots of external Ca^{2+} block

Dose-inhibition curves of external Ca^{2+} block were fit using a single binding site isotherm function as described previously[68]:

$$G = G_{min} + \frac{1 - G_{min}}{1 + \left(\frac{[Ca]}{IC_{50}}\right)^{N}} \quad (5)$$

Where IC_{50} is the concentration of external Ca^{2+} that elicits half-maximal block, N is the slope and G_{min} is the steady-state response.

Statistics

Results are expressed as mean ± s.e.m. Values for n refer to the number of individual patches. Statistical analyses were performed using Origin Pro 2020 (OriginLab). Two-tailed unpaired t-test with Welch correction was performed on the populations for which the normal distribution assumption could not be rejected (Shapiro–Wilk analyses, $P > 0.15$; Figs. 5e,f and 6d). Mann–Whitney U-test was performed on the population that was not normally distributed (Fig. 5d). $P < 0.05$ was considered to be statistically significant. *** indicates $P < 0.001$.

All data were illustrated using Origin Pro 2020 and Adobe Illustrator CS5.

Reporting summary

Further information on research design is available in the Nature Portfolio Reporting Summary linked to this article.

Data availability

The structural data in this work have been deposited in the Protein Data Bank (PDB) and the Electron Microscopy Data Bank (EMDB) under the accession numbers PDB 8FQF (EMD-29386), PDB 8FP9 (EMD-29360), PDB 8FQ1 (EMD-29737), PDB 8FP4 (EMD-29359), PDB 8FQB (EMD-29382), PDB 8FQ5 (EMD-29378), PDB 8FPS (EMD-29369), PDB 8FPG (EMD-29363), PDB 8FQG (EMD-29387), PDB 8FQH (EMD-29388), PDB 8FQ0 (EMD-29394), PDB 8FPC (EMD-29361), PDB 8FPH (EMD-29364), PDB 8FQ6 (EMD-29379), PDB 8FPV (EMD-29370), PDB 8FPY (EMD-29371), PDB 8FPZ (EMD-29372), PDB 8FQD (EMD-29384), PDB 8FQE (EMD-29385), PDB 8FQ8 (EMD-29380), PDB 8FQA (EMD-29381), PDB 8FQ2 (EMD-29375), PDB 8FQ3 (EMD-29376), PDB 8FPK (EMD-29367) and PDB 8FPL (EMD-29368). The C1 maps are associated with each entry. Request for materials (plasmids and cell lines) will be fulfilled for reasonable inquiries and should be addressed to the corresponding author. Source data are provided with this paper.

References

52. Shanks, N. F., Maruo, T., Farina, A. N., Ellisman, M. H. & Nakagawa, T. Contribution of the global subunit structure and stargazin on the maturation of AMPA receptors. *J. Neurosci.* **30**, 2728–2740 (2010).
53. Nakagawa, T. Structures of the AMPA receptor in complex with its auxiliary subunit cornichon. *Science* **366**, 1259–1263 (2019).
54. Farina, A. N. et al. Separation of domain contacts is required for heterotetrameric assembly of functional NMDA receptors. *J. Neurosci.* **31**, 3565–3579 (2011).
55. Zivanov, J. et al. New tools for automated high-resolution cryo-EM structure determination in RELION-3. *eLife* **7**, e42166 (2018).
56. Zheng, S. Q. et al. MotionCor2: anisotropic correction of beam-induced motion for improved cryo-electron microscopy. *Nat. Methods* **14**, 331–332 (2017).
57. Rohou, A. & Grigorieff, N. CTFFIND4: fast and accurate defocus estimation from electron micrographs. *J. Struct. Biol.* **192**, 216–221 (2015).
58. Warshamanage, R., Yamashita, K. & Murshudov, G. N. EMDA: a Python package for electron microscopy data analysis. *J. Struct. Biol.* **214**, 107826 (2022).
59. Kucukelbir, A., Sigworth, F. J. & Tagare, H. D. Quantifying the local resolution of cryo-EM density maps. *Nat. Methods* **11**, 63–65 (2014).
60. Rosenthal, P. B. & Henderson, R. Optimal determination of particle orientation, absolute hand, and contrast loss in single-particle electron cryomicroscopy. *J. Mol. Biol.* **333**, 721–745 (2003).
61. Pettersen, E. F. et al. UCSF Chimera—a visualization system for exploratory research and analysis. *J. Comput. Chem.* **25**, 1605–1612 (2004).
62. Emsley, P., Lohkamp, B., Scott, W. G. & Cowtan, K. Features and development of Coot. *Acta Crystallogr. D* **66**, 486–501 (2010).
63. Afonine, P. V. et al. Real-space refinement in PHENIX for cryo-EM and crystallography. *Acta Crystallogr. D* **74**, 531–544 (2018).
64. Klesse, G., Rao, S., Sansom, M. S. P. & Tucker, S. J. CHAP: a versatile tool for the structural and functional annotation of ion channel pores. *J. Mol. Biol.* **431**, 3353–3365 (2019).
65. Sievers, F. et al. Fast, scalable generation of high-quality protein multiple sequence alignments using Clustal Omega. *Mol. Syst. Biol.* **7**, 539 (2011).
66. Brown, P. M., Aurousseau, M. R., Musgaard, M., Biggin, P. C. & Bowie, D. Kainate receptor pore-forming and auxiliary subunits regulate channel block by a novel mechanism. *J. Physiol.* **594**, 1821–1840 (2016).
67. Dawe, G. B. et al. Nanoscale mobility of the apo state and TARP stoichiometry dictate the gating behavior of alternatively spliced AMPA receptors. *Neuron* **102**, 976–992.e5 (2019).
68. Wong, A. Y., Fay, A. M. & Bowie, D. External ions are coactivators of kainate receptors. *J. Neurosci.* **26**, 5750–5755 (2006).

Acknowledgements

We acknowledge the use of the cryo-EM facility at the Center for Structural Biology and DORS Data Storage Core at Vanderbilt University. M. Chambers, S. Collier and M. Haider maintained the cryo-EM facility and facilitated data collection. We thank K. Kim and P. Christov at Vanderbilt Chemical Synthesis Core for synthesizing chemicals. Software was provided by SBGrid. The work was supported by funding from a National Institutes of Health grant R56/R01MH123474 (to T.N.), S10OD030292-01 (to T.N), Stanley Cohen Innovation Fund (to T.N.) and the Canadian Institutes of Health Research (FRN 163317, D.B.). X.-t.W. was funded by a Max Binz fellowship from McGill University's Faculty of Medicine.

Author contributions

T.N. conceived the project, conducted cryo-EM experiments and pilot electrophysiology experiments, analyzed data and wrote the paper with inputs from other authors. D.B. provided insights into the divalent cation block and supervised electrophysiology experiments. X.-t.W. and F.J.M.-C. conducted electrophysiology experiments and analyzed data. T.N. and D.B. provided funding.

Competing interests

The authors declare no competing interests.

Additional information

Extended data is available for this paper at https://doi.org/10.1038/s41594-024-01228-3.

Supplementary information The online version contains supplementary material available at https://doi.org/10.1038/s41594-024-01228-3.

Correspondence and requests for materials should be addressed to Terunaga Nakagawa.

Peer review information *Nature Structural & Molecular Biology* thanks Janesh Kumar and the other, anonymous, reviewer(s) for their contribution to the peer review of this work. Peer reviewer reports are available. Primary Handling Editor: Sara Osman, in collaboration with the *Nature Structural & Molecular Biology* team.

https://doi.org/10.1038/s41594-024-01228-3

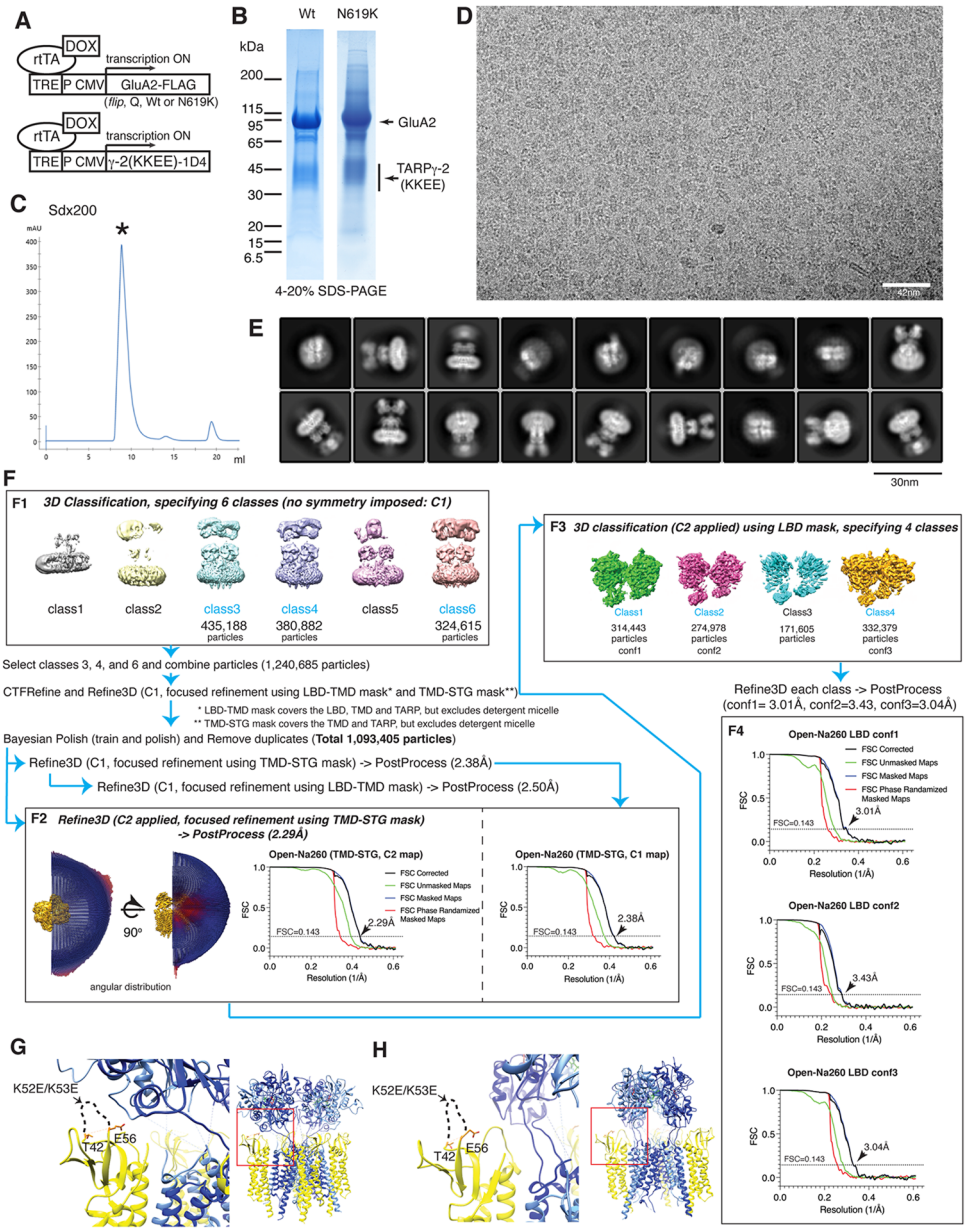

Extended Data Fig. 1 | Expression, purification, and cryo-EM data processing. **A**. DOX inducible expression scheme used in stable HEK cell line. In clone #53, GluA2(*flip*-Q isoform) and TARPγ-2(KKEE) were stably co-expressed, independently without tether. Clone #8 expresses the GluA2(*flip*-Q isoform, N619K mutant) and TARPγ2(KKEE). TARPγ2 is abbreviated as γ-2. **B**. Purified complex resolved in SDS-PAGE. **C**. Superdex200 (Sdx200) size exclusion chromatograph in the final step of purification. The peak with asterisk contains the complex formed of GluA2(*flip*-Q) and TARPγ2(KKEE). The N619K mutant complex exhibit identical chromatography profile and not shown. **D**. A representative motion corrected cryo-EM image of purified GluA2/TARPγ2(KKEE) complex of Open-Na260. The displayed image is representative among a total of ~16,000 micrographs. **E**. A set of representative 2D class averages obtained during the image processing of Open-Na260. The class averages displayed are from 1/4 of the total dataset. **F**. Image processing of Open-Na260. Other structures were obtained using similar procedures and described in the methods. **G-H**. The atomic model of Open-Na260. GluA2=blue, TARPγ2(KKEE)=yellow. TARPγ2(KKEE) in the A′/C′ positions (G) and B′/D′ positions (H) are shown. The zoomed views (left panels) correspond to the red square in the right panels. In all the structures determined in this work (see Table1), the regions containing the KKEE mutations were unresolved due to structural flexibility of the extracellular loop.

https://doi.org/10.1038/s41594-024-01228-3

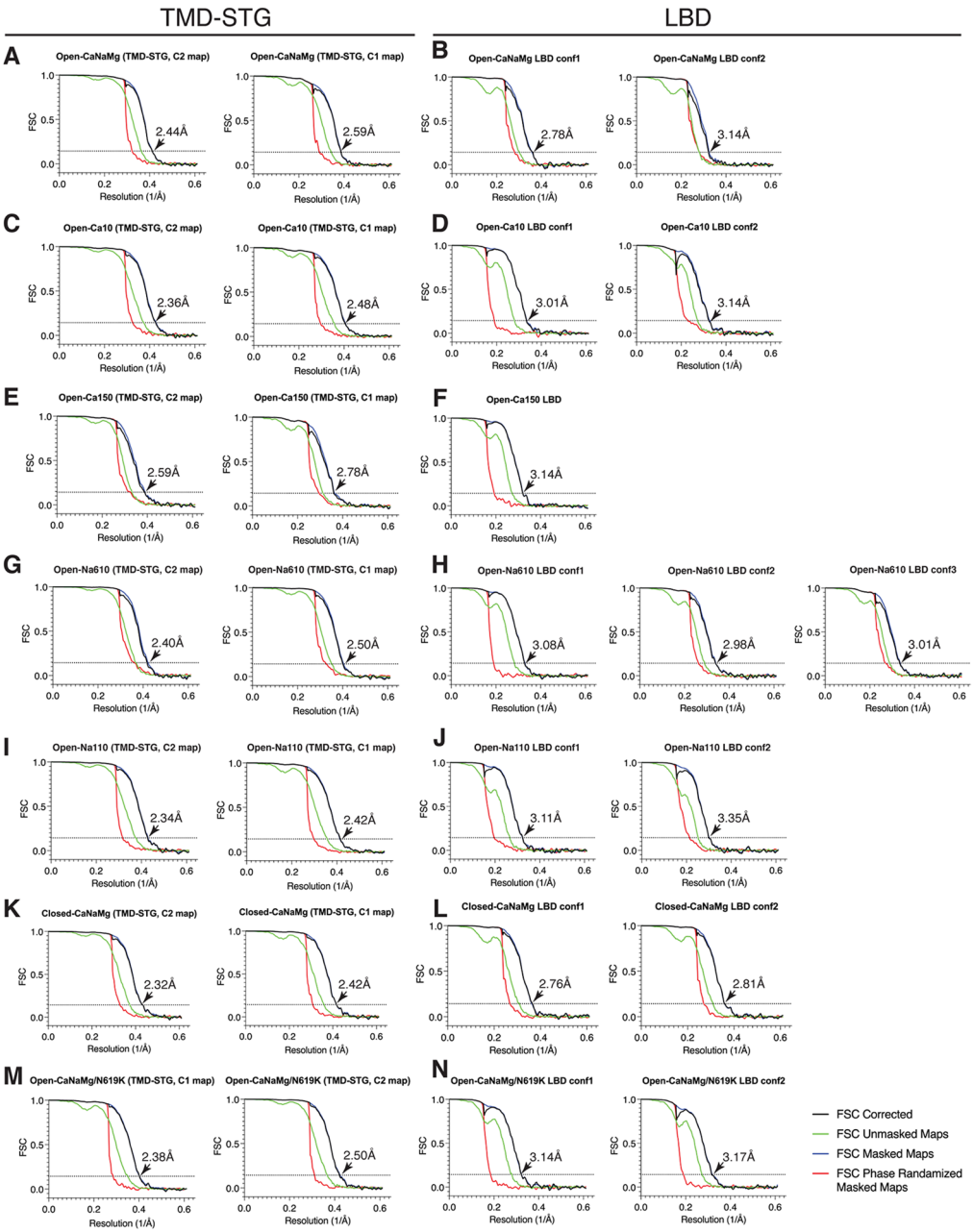

Extended Data Fig. 2 | Fourier Shell Correlation (FSC) curves. The FSC curves of the GluA2/TARP complexes presented in this work. The membrane embedded portion of the structures were refined using the TMD-STG mask, with (C2) and without (C1) imposing symmetry (**A, C, E, G, I, K, and M**). The LBDs were refined using the LBD mask with C2 symmetry imposed (**B, D, F, H, J, L, and N**). **A-B**. Open-CaNaMg. **C-D**. Open-Ca10. **E-F**. Open-Ca150. G-H. Open-Na610. I-J. Open-Na110. **K-L**. Open-CaNaMg/N619K. **M-N**. Closed-CaNaMg. The FSCs and final resolutions were calculated using Relion. FSC = 0.143 is indicated by dashed line. Resolution is indicated by the arrows and numbers. Note: FSC curves of Open-Na260 are provided in Extended Data Fig. 1F2 and F4.

https://doi.org/10.1038/s41594-024-01228-3

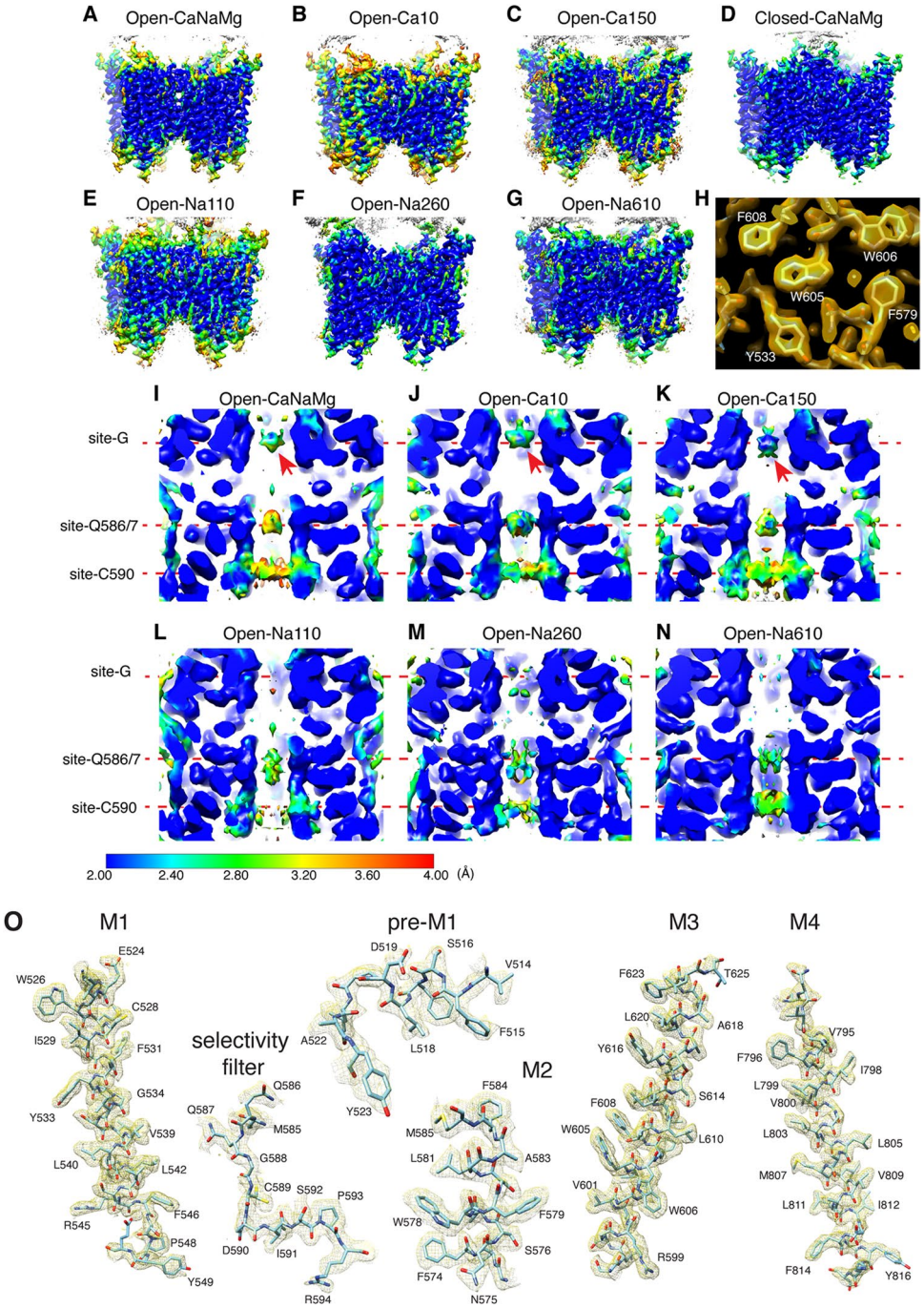

Extended Data Fig. 3 | Local resolution and representative fit between map and model. A-G. Local resolution was estimated by ResMap[59], using as input the half-maps generated by 3D refinement in Relion. The heatmap for resolution is shown on the bottom right. Side view of each indicated structure. **H.** Overlay of map and model in a subregion of M1-3 helices. With an optimal threshold, the holes in the aromatic sidechains are discernable. **I-N.** Cross sections of local resolution heatmaps of the open pores. The arrows in **I-K** are the Ca^{2+} density at site−G. Note higher local resolution of the density in 150 mM Ca^{2+} (Open-Ca150) compared to 10 mM Ca^{2+} (Open-Ca10 and Open-CaNaMg), consistent with more binding at higher concentration. Note, the maps displayed are half-maps that are unfiltered/unsharpened, and thus the resolution appear lower than the full-maps displayed in other figures. **O.** Representative overlay of map and model in the TMD. Open-Na260 is shown. Others were at similar quality. Also see Extended Data Figs. 6–8.

https://doi.org/10.1038/s41594-024-01228-3

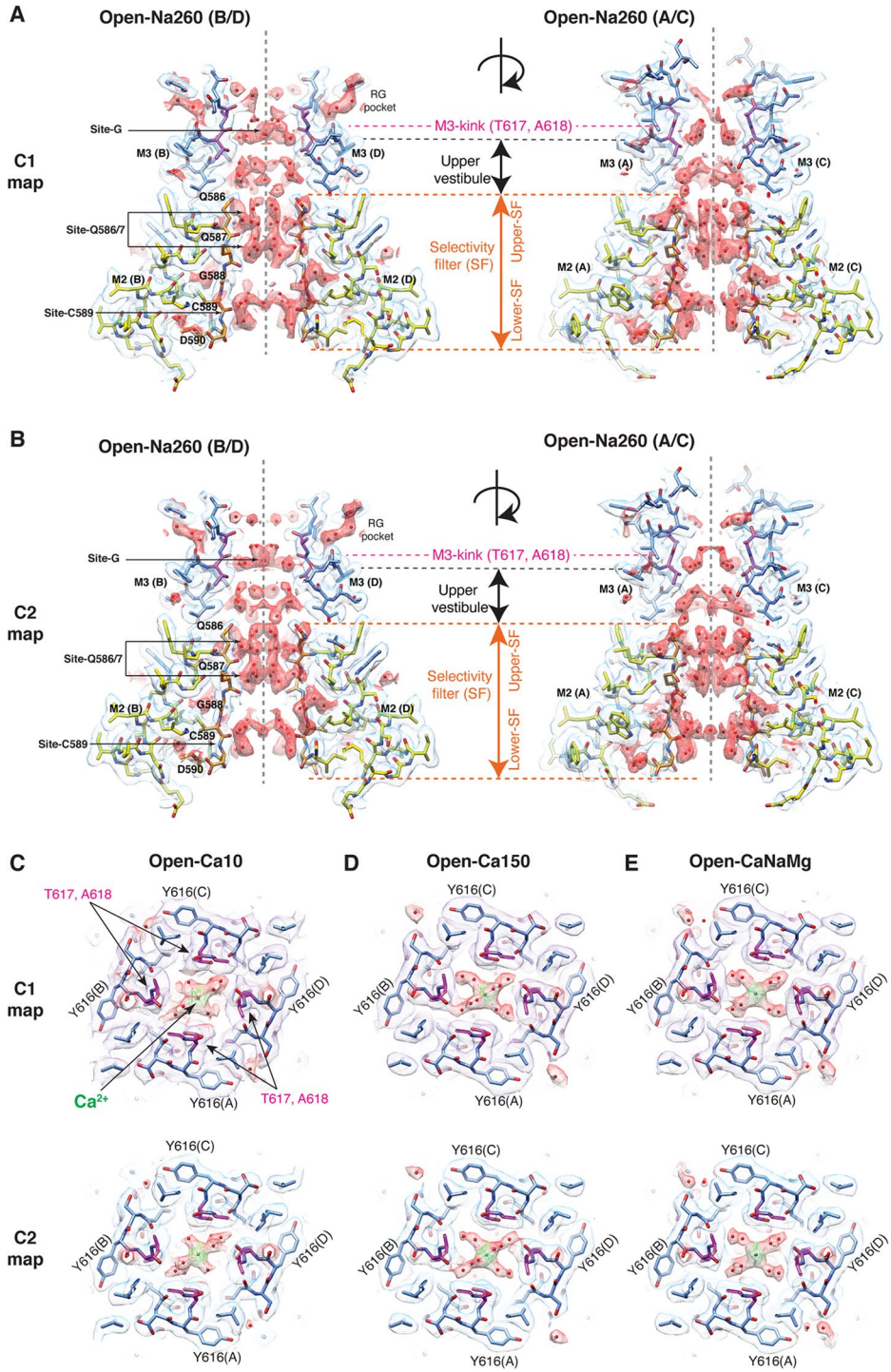

Extended Data Fig. 4 | Consistency of pore densities between the C1 and C2 maps. A-B. Cross sections of the pores of Open-Na260. (A) C1 maps. (B) C2 maps. All maps were filtered according to the local resolution calculated by Relion. The cryo-EM density map (mesh) and the atomic model are superimposed. The atomic models were built based on the C2 map and superimposed into the C1 map in A. Putative water and calcium ion are in red mesh. The atomic models of the polypeptides of M2, SF, and M3 are shown in yellow, orange, and sky blue, where elements are colored according to oxygen=red, nitrogen=blue, and sulfate=yellow. Resides that define the gate in the M3 of each structure are colored magenta. **C-E**. Overlay of the model and map at site^{-}G are shown. **C**. Open-Ca10. **D**. Open-Ca150. **E**. Open-CaNaMg. Top: C1 map. Bottom: C2 map. The C1 map was filtered using the local resolution function in Relion. T617 and A618 are in magenta. The Ca^{2+} is green.

https://doi.org/10.1038/s41594-024-01228-3

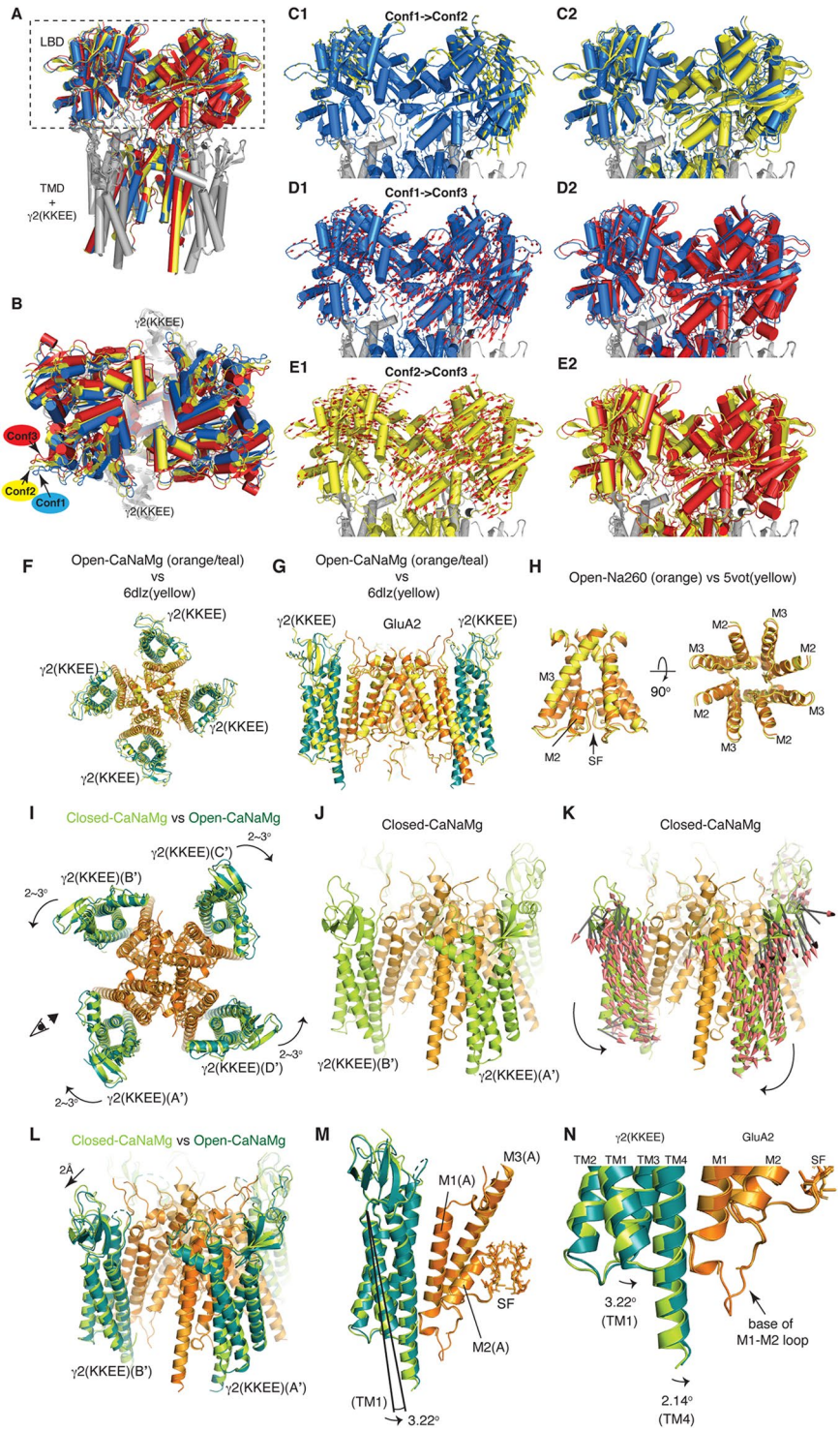

Extended Data Fig. 5 | See next page for caption.

https://doi.org/10.1038/s41594-024-01228-3

Extended Data Fig. 5 | Global structures of the A2iQ/γ2(KKEE). **A-E**. Conformational heterogeneity of the LBD gating ring in Open-Na260. **A**. LBD-TMD sectors were reconstructed from particles that produced LBD Conf1, Conf2, and Conf3. The LBD-TMD were aligned and superimposed using the cytoplasmic half of the SF. The TMD and γ2(KKEE) are nearly perfectly aligned as expected; there was no obvious global conformational heterogeneity of the TMD and γ2(KKEE). Blue=Conf1, Yellow=Conf2, and Red=Conf3. The rectangle indicates the regions that are highlighted in panels C-E. **B**. The LBD gating ring of the aligned and superimposed structure shown in panel A is viewed from above. The helices of the LBDs do not superimpose. **C**. Conformational transition from Conf1 to Conf2. The Conf1 conformation is shown with the mode vectors (yellow arrows) that schematically represent the displacements of the Cα during the conformational transition from Conf1 to Conf2 (panel C1). The lengths of the vectors are increased by 50% than actual displacements for clarity. The Conf1 and Conf2 conformations are superimposed in the same view as in panel C1. **D** and **E**. The transition from Conf1 to Conf3 (panels D1 and D2) and from Conf2 to Conf3 (panels E1 and E2) are shown as in panel C. **F-N**. Global architecture of A2iQ/γ-2(KKEE). **F** and **G**. The atomic model of Open-CaNaMg at 2.4 Å resolution, where γ2(KKEE) in teal and GluA2 in orange, is superimposed to the A2iQ/γ2 wild-type complex in yellow (PDB:6dlz, 3.9 Å resolution). The root mean square deviation (RMSD) of the Cα is 1.909 Å. Top view (A) and cross section side view (B). **H**. The pore (that is, M2, SF, and M3) of Open-Na260 at 2.3 Å resolution is superimposed to the A2iQ/γ2 wild-type complex in yellow (PDB:5vot, 4.9 Å resolution). The RMSD of Cα of the M3 in B/D subunit pairs is 0.642 Å. **I**. Conformational difference between Closed-CaNaMg and Open-CaNaMg. The two structures were aligned at the cytoplasmic half of M3 (residue 597-610) at RMSD = 0.3 Å. GluA2 are colored in ogrange and light orange in Open-CaNaMg and Closed-CaNaMg, respectively. The four γ2(KKEE)s of Open-CaNaMg are colored in teal, and in Closed-CaNaMg they are in light green. The position of the γ2(KKEE)s relative to the GluA2 are indicated by the A′-D′ labels, as defined in Fig. 1B. The γ2(KKEE)s undergo counter rotations of 2-3° within the A′/B′ and C′/D′ pairs (curved arrows). The eye and arrow indicate the viewpoint of the structures in J-K. **J**. Closed-CaNaMg without the mode vector arrows. **K**. Closed-CaNaMg with the mode vector arrows that describe the directions and magnitudes of displacement of the Cα between Closed-CaNaMg and Open-CaNaMg. Arrows are shown for all motion greater than 0.5 Å. The counter rotation of the γ2(KKEE)s in the A′/B′ pairs are shown. **L**. Superposition of the Open-CaNaMg and Closed-CaNaMg shows the ~2 Å outward motion of the extracellular domain of the TARPs. **M** and **N**. The activation is also accompanied by a 2-3° tilt of the TARPs, which brings close the cytoplasmic extension of TM4 of γ2(KKEE) to the base of M1-M2 loop of GluA2. In the magnified view (I), the difference in the tilt angle in TM1 and TM4 of γ2(KKEE) is shown.

https://doi.org/10.1038/s41594-024-01228-3

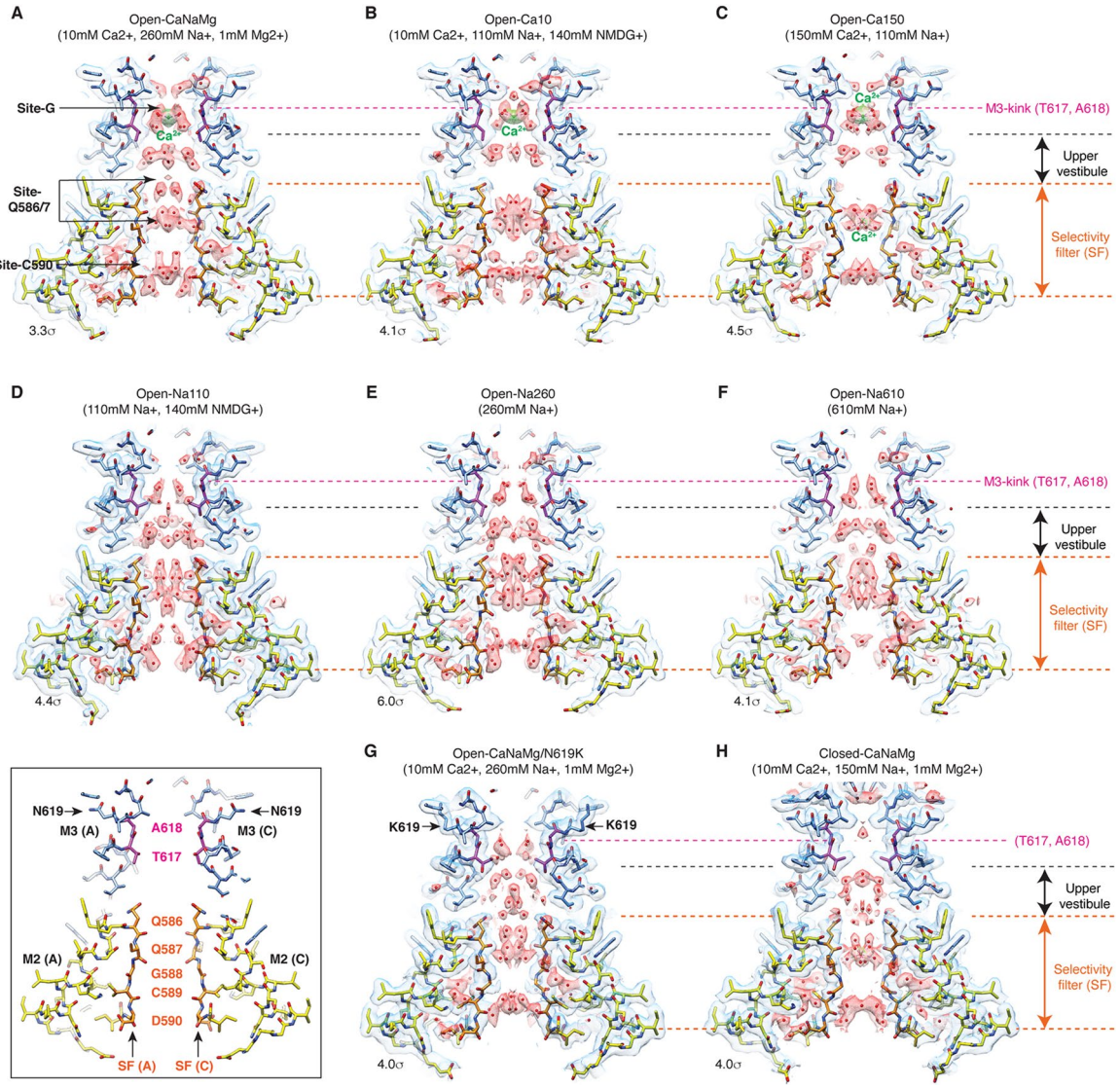

Extended Data Fig. 6 | Comparison of cryo-EM maps and models in the pores in the cross-section containing the A/C subunits. Cross sections containing A/C subunits of the pores of Open-CaNaMg (**A**), Open-Ca10 (**B**), Open-Ca150 (**C**), Open-Na110 (**D**), Open-Na260 (**E**), Open-Na610 (**F**), Open-CaNaMg/N619K (**G**), and Closed-CaNaMg (**H**) are displayed. The cryo-EM density map (mesh) and the atomic model are superimposed. The cryo-EM maps are displayed using the indicated sigma values. Putative water and calcium ion are in red and green spheres, respectively. The atomic models of the polypeptides of M2, SF, and M3 are shown in yellow, orange, and sky blue, where elements are colored according to oxygen=red, nitrogen=blue, and sulfate=yellow. Resides that define the gate in the M3 of each structure are colored magenta. The left bottom inset shows the locations of the key residues in the wild type open pore. C2 maps are displayed (also see Table 1).

https://doi.org/10.1038/s41594-024-01228-3

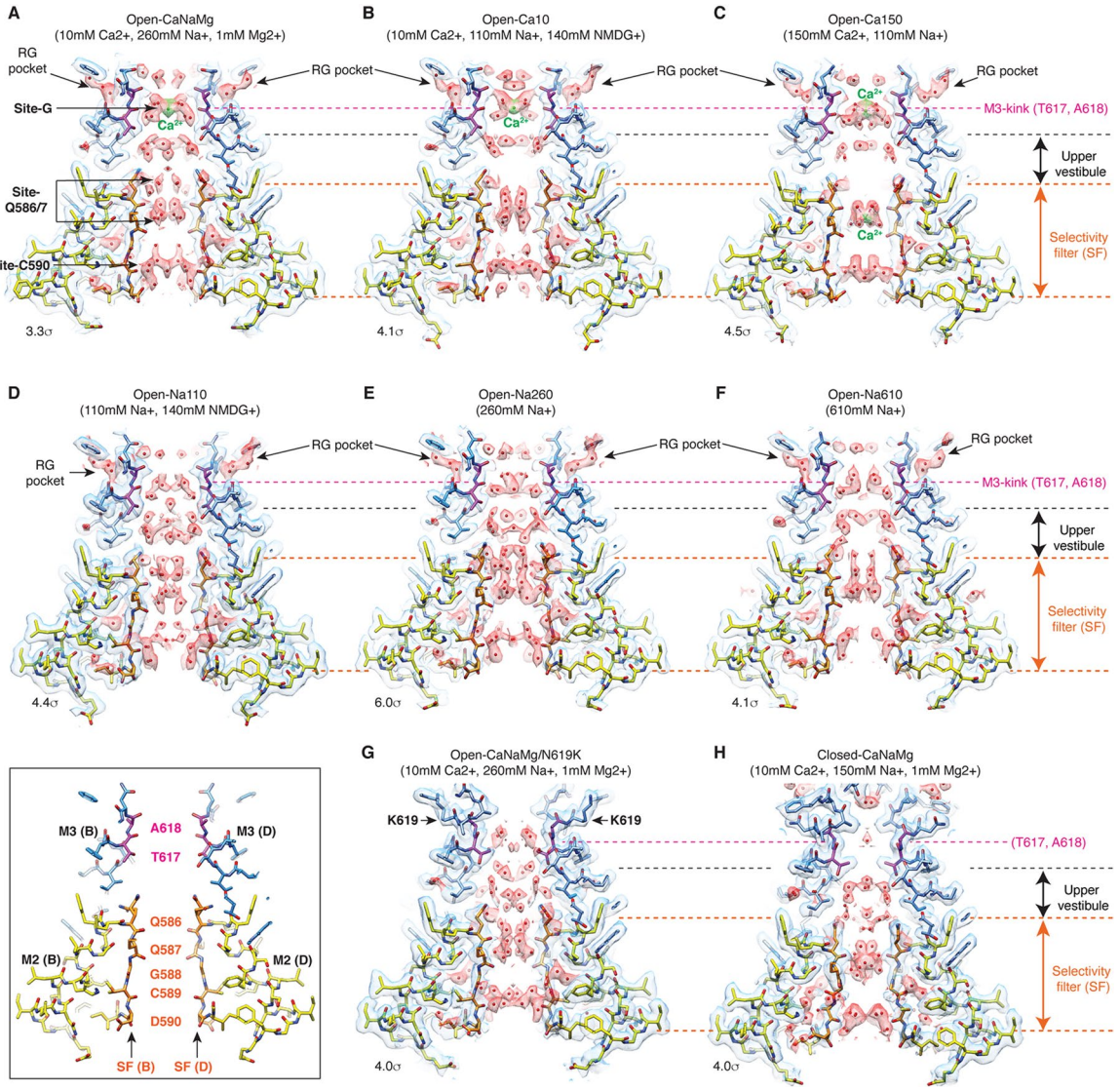

Extended Data Fig. 7 | Comparison of cryo-EM maps and models in the pores in the cross-section containing the B/D subunits. Cross sections containing B/D subunits of the pores of Open-CaNaMg **(A)**, Open-Ca10 **(B)**, Open-Ca150 **(C)**, Open-Na110 **(D)**, Open-Na260 **(E)**, Open-Na610 **(F)**, Open-CaNaMg/N619K **(G)**, and Closed-CaNaMg **(H)** are displayed. The cryo-EM density map (mesh) and the atomic model are superimposed. The cryo-EM maps are displayed using the indicated sigma values. Putative water and calcium ion are in red and green spheres, respectively. The atomic models of the polypeptides of M2, SF, and M3 are shown in yellow, orange, and sky blue, where elements are colored according to oxygen=red, nitrogen=blue, and sulfate=yellow. Resides that define the gate in the M3 of each structure are colored magenta. The left bottom inset shows the locations of the key residues in the wild type open pore. Each view is the orthogonal to the corresponding structure shown in the previous figure. C2 maps are displayed (also see Table 1).

https://doi.org/10.1038/s41594-024-01228-3

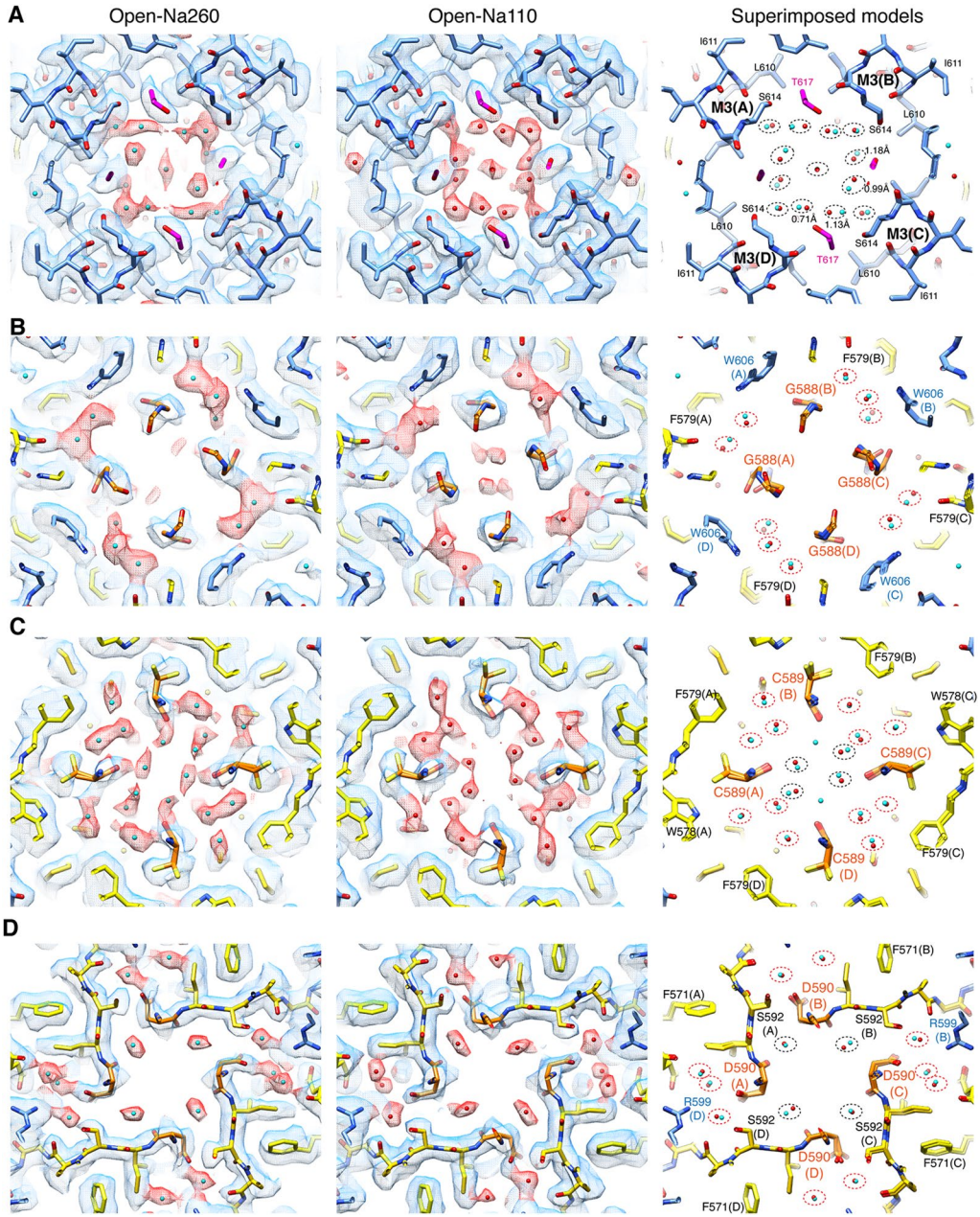

Extended Data Fig. 8 | Putative water in the vestibules that are common in Open-Na260 and Open-Na110. The horizontal sections through the upper **(A)** and lateral vestibule (B-D). The sections were made at different levels that contain residue S614 **(B)**, G588 (B), C589 **(C)**, and D590 **(D)** of the SF. In each row, Open-Na260 (left), Open-Na110 (middle), and superimposed models of two structures are displayed. Blue and red mesh are density map of polypeptides and putative water, respectively. The M3 (blue model), M2 with M2-M3 linker (yellow model), and SF (orange model) are shown. Cyan and red spheres are putative water in Open-Na260 and Open-Na110, respectively. The location of putative water is nearly identical in both structures, as indicated by dotted ovals surrounding the cyan and red water pairs in the right panels. The water surrounded by the red dashed oval are the ones in the lateral vestibules. Cyan-red sphere pair distances were below 1 Å in most cases. In A (right) the actual distances are provided next to the oval for subset of cyan-red sphere pairs. The densities in the lateral vestibule interpreted as water, described above, are unlikely to be cation because these is always a nearby -NH group within 3 Å distance.

https://doi.org/10.1038/s41594-024-01228-3

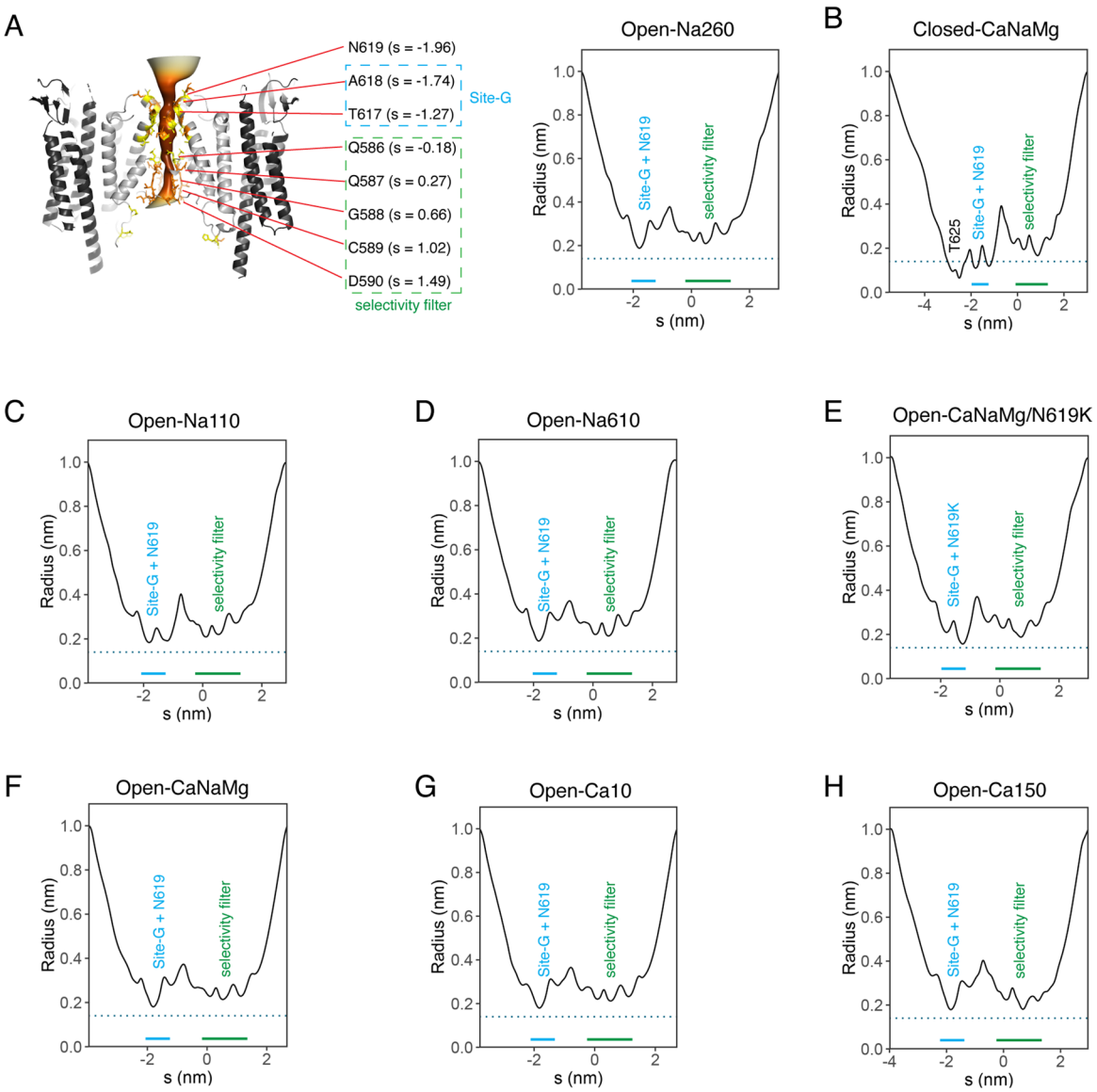

Extended Data Fig. 9 | Solvent accessible pore radius. The pore radius accessible to solvent was estimated using CHAP software[64]. **A**. (Left) The surface representation of the accessible pore is shown with the ribbon diagram of Open-Na260. GluA2: light gray. TARPγ-2: dark gray. Pore facing and pore lining residues are in yellow and orange, respectively. The darkness of orange surface corelates with narrower radius of the pore. The value of s is the coordinate along the pore pathway, whose origin is set at the center of mass of the pore forming residues. The relations between the key pore residues and the value of s (in the unit of nm) are shown. (right) Radius vs. s plot. The location of the site-G plus N619 (or N619K) and SF are in blue and green, respectively. The dashed line indicates 1.4 Å. The radius of closed pore (Closed-CaNaMg) plotted in B crosses below the 1.4 Å radius but the open pores don't. Radius vs. s plots are shown for Open-Na110 (C), Open-Na610 (D), Open-CaNaMg/N619K (E), Open-CaNaMg (F), Open-Ca10 (G), and Open-Ca150 (H).

https://doi.org/10.1038/s41594-024-01228-3

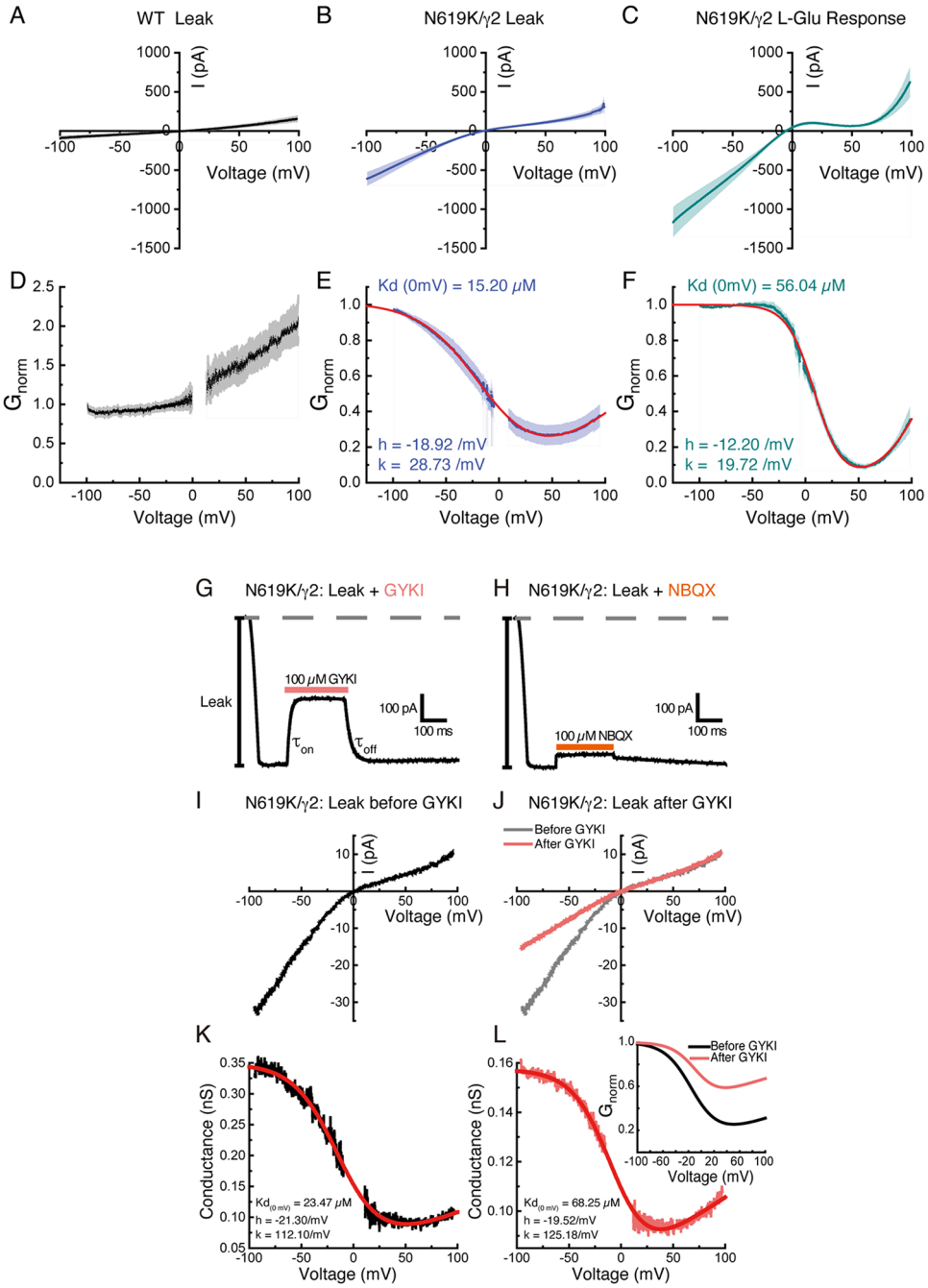

Extended Data Fig. 10 | Characterization of A2iQ(N619K)/γ2 complex. **A-C**. Averaged ramp currents (I-V) recorded in excised patches expressing wild-type A2iQ/γ2 prior to agonist stimulation (**A**, black), N619K/γ2 leak (**B**, blue) and agonist-evoked (**C**, dark cyan) responses using an internal patch solution containing 30 μM spermine. Dim colours show the SEM. The I-V plots both show bi-rectifying I-V relationships demonstrating that cytoplasmic spermine blocks the leak (**B**) and agonist-gated state (**C**) of the mutant A2iQ(N619K)/γ2 receptors. Data are presented as mean values ± SEM. (also see Supplementary Table 4). **D-F**. Conductance-voltage (G-V) plots converted from **A-C** for wild-type leak (**D**, black), N619K/γ2 leak (**E**, blue) and agonist-evoked (**F**, dark cyan) responses. In dim colours it is shown the SEM of the averaged conductance curves, respectively. Red lines in **E** and **F** are the fit for the G-V relationships for leak and agonist-evoked responses of N619K/γ2 receptors, respectively, using the single permeant blocker model (Eq. 1). Data are presented as mean values ± SEM. (Also see Supplementary Table 7) **G** and **H**. Fast jumps experiments comparing the ability of the AMPAR negative allosteric modulator, GYKI 52466 (100 μM) (**G**, Patch # 221129p3) or the competitive antagonist, NBQX (100 μM) (**H**, Patch # 221129p3) to block the leak currents mediated by N619K/γ2 receptors. The onset and off kinetics of GYKI (**G**) were estimated as τ_{on} = 12.7 ± 0.9 ms (n = 10) and τ_{off} = 37.1 ± 3.9 ms (n = 10), respectively (also see Supplementary Table 5 and 6). **I**. I-V plot of the leak current of N619K/γ2 receptors with an internal patch solution containing 30 μM spermine in the absence of agonist. **J**. Typical I-V plots of leak currents of N619K/γ2 receptors before (grey) and after (pink) applying 100 μM GYKI (Patch # 221201p4), in the absence of agonist and containing 30 μM spermine in the internal solution. **K** and **L**. Conductance-voltage (G-V) plots of the leak N619K/γ2 receptors, converted from **J** (Patch # 221201p4), before (**K**, black) and after (**L**, pink) applying 100 μM GYKI. The G-V curves are fit (red in **K** and **L**) using a single permeant ion blocker model (Eq. 1). **L**. (inset) Normalized G-V plots before (black) and after (pink) the application of GYKI are superimposed.

nature portfolio

Corresponding author(s): Terunaga Nakagawa

Last updated by author(s): 11/22/2023

Reporting Summary

Nature Portfolio wishes to improve the reproducibility of the work that we publish. This form provides structure for consistency and transparency in reporting. For further information on Nature Portfolio policies, see our Editorial Policies and the Editorial Policy Checklist.

Statistics

For all statistical analyses, confirm that the following items are present in the figure legend, table legend, main text, or Methods section.

n/a	Confirmed	
☐	☒	The exact sample size (*n*) for each experimental group/condition, given as a discrete number and unit of measurement
☐	☒	A statement on whether measurements were taken from distinct samples or whether the same sample was measured repeatedly
☐	☒	The statistical test(s) used AND whether they are one- or two-sided *Only common tests should be described solely by name; describe more complex techniques in the Methods section.*
☒	☐	A description of all covariates tested
☐	☒	A description of any assumptions or corrections, such as tests of normality and adjustment for multiple comparisons
☐	☒	A full description of the statistical parameters including central tendency (e.g. means) or other basic estimates (e.g. regression coefficient) AND variation (e.g. standard deviation) or associated estimates of uncertainty (e.g. confidence intervals)
☐	☒	For null hypothesis testing, the test statistic (e.g. *F*, *t*, *r*) with confidence intervals, effect sizes, degrees of freedom and *P* value noted *Give P values as exact values whenever suitable.*
☒	☐	For Bayesian analysis, information on the choice of priors and Markov chain Monte Carlo settings
☒	☐	For hierarchical and complex designs, identification of the appropriate level for tests and full reporting of outcomes
☒	☐	Estimates of effect sizes (e.g. Cohen's *d*, Pearson's *r*), indicating how they were calculated

Our web collection on statistics for biologists contains articles on many of the points above.

Software and code

Policy information about availability of computer code

Data collection	EPU v2.6-3.3 (Thermofisher Scientific), pClamp10 (Molecular Devices)
Data analysis	Relion v3 (open source), CTFFIND4 (open source), motioncorr2 (open source), Resmap v1.95 (open source), coot v0.897 (for OSX, open source), chimera v1.14 (open source) , pymol v2.1 (Schrodinger), phenix v1.20 (open source), Origin Pro 2020 (Originlab), Microsoft Excel v16 (Microsoft), Prism v9 (Graph Pad Software)

For manuscripts utilizing custom algorithms or software that are central to the research but not yet described in published literature, software must be made available to editors and reviewers. We strongly encourage code deposition in a community repository (e.g. GitHub). See the Nature Portfolio guidelines for submitting code & software for further information.

Data

Policy information about availability of data

All manuscripts must include a data availability statement. This statement should provide the following information, where applicable:

- Accession codes, unique identifiers, or web links for publicly available datasets
- A description of any restrictions on data availability
- For clinical datasets or third party data, please ensure that the statement adheres to our policy

The structural data in this work is deposited to PDB (and EMDB) under the accession numbers: 8FQF(EMD-29386), 8FP9(EMD-29360), 8FQ1(EMD-29737), 8FP4(EMD-29359), 8FQB(EMD-29382), 8FQ5(EMD-29378), 8FPS(EMD-29369), 8FPG(EMD-29363), 8FQG(EMD-29387), 8FQH(EMD-29388), 8FQ0(EMD-29394),

8FPC(EMD-29361), 8FPH(EMD-29364), 8FQ6(EMD-29379), 8FPV(EMD-29370), 8FPY(EMD-29371), 8FPZ(EMD-29372), 8FQD(EMD-29384), 8FQE(EMD-29385), 8FQ8(EMD-29380), 8FQA(EMD-29381), 8FQ2(EMD-29375), 8FQ3(EMD-29376), 8FPK(EMD-29367), 8FPL(EMD-29368). The C1 maps are associated with each entry. Request for materials (plasmids and cell lines) will be fulfilled for reasonable inquiries and should be addressed to Terunaga Nakagawa.

Research involving human participants, their data, or biological material

Policy information about studies with human participants or human data. See also policy information about sex, gender (identity/presentation), and sexual orientation and race, ethnicity and racism.

Reporting on sex and gender	n/a
Reporting on race, ethnicity, or other socially relevant groupings	n/a
Population characteristics	n/a
Recruitment	n/a
Ethics oversight	n/a

Note that full information on the approval of the study protocol must also be provided in the manuscript.

Field-specific reporting

Please select the one below that is the best fit for your research. If you are not sure, read the appropriate sections before making your selection.

☒ Life sciences ☐ Behavioural & social sciences ☐ Ecological, evolutionary & environmental sciences

For a reference copy of the document with all sections, see nature.com/documents/nr-reporting-summary-flat.pdf

Life sciences study design

All studies must disclose on these points even when the disclosure is negative.

Sample size	Sample size for cryo-EM data collection was determined based on the knowledge that AMPARs require about hundred thousand particles to reach 3.5Å resolution. To achieve sub-2.5Å in both C1 and C2 map we found that about 500,000 to 1,000,000 particles are needed, which translates into collecting 16,000 to 34,000 micrographs. The sample sizes of electrophysiolgy experiments follow previous studies in the field that investigated divalent cation block, gating kinetics, and calcium permeability.
Data exclusions	CTF and rlnMaxResolution parameters were used to remove images with bad image quality. 3D classification removes particles based on objective statistical measures which retains particles with homogeneous structures containing high resolution signals. Patches that exhibit slow open tip response after breaking the patch were interpreted as compromised solution exchange and excluded from the analysis.
Replication	Expression and purification were highly robust and reproducible across experiments. The half maps of the 3D refinement in each structure produced consistent results, which supports high consistency of data quality across micrographs. The C1 and C2 maps were also consistent, justifying the use of C2 symmetry. To definitively identify calcium ions, cryo-EM experiments were conducted with 6 different ionic conditions. Ca2+ was density was reproduced in three cases where Ca2+ was present in the buffer, but not in the remaining three conditions that lacks Ca2+. All data points were used in the current recordings. Under our experimental condition, the gating properties of the wild type AMAPR/TARPgamma2, which is used as baseline controls, were highly reproducible and consistent with previously published results in the field.
Randomization	Resolution estimate in cryo-EM was conducted using reconstructions obtained from two datasets that are generated by randomly splitting the full-dataset into two halves. Membrane patches were pulled from randomly selected cells within those that expressed the transfected proteins.
Blinding	The experimenters were not blinded about the information of the samples they were handling.

Reporting for specific materials, systems and methods

We require information from authors about some types of materials, experimental systems and methods used in many studies. Here, indicate whether each material, system or method listed is relevant to your study. If you are not sure if a list item applies to your research, read the appropriate section before selecting a response.

Materials & experimental systems

n/a	Involved in the study
☐	☒ Antibodies
☐	☒ Eukaryotic cell lines
☒	☐ Palaeontology and archaeology
☒	☐ Animals and other organisms
☒	☐ Clinical data
☒	☐ Dual use research of concern
☒	☐ Plants

Methods

n/a	Involved in the study
☒	☐ ChIP-seq
☒	☐ Flow cytometry
☒	☐ MRI-based neuroimaging

Antibodies

Antibodies used	anti-FLAG M2 monoclonal antibody
Validation	Purchased from Sigma. The product is quality controlled.

Eukaryotic cell lines

Policy information about cell lines and Sex and Gender in Research

Cell line source(s)	TetON HEK cell (Clontech) and their derivatives isolated in Nakagawa lab.
Authentication	The cell line was purchased from Clontech. The cell morphology is spindle shaped and homogeneous. Growth rate was consistent with HEK cell. The cell line respond to DOX as described by the manufacturer. The cell line is sensitive to hygromycine and zeocin. he cell line is insensitive to G418. The line is used extensively in past literatures to generate stable cell lines that DOX dependently express proteins for structural studies.
Mycoplasma contamination	Not tested. We use FCS that are mycoplsma negative for culturing the line.
Commonly misidentified lines (See ICLAC register)	n/a